ISPRS Journal of Photogrammetry and Remote Sensing 210 (2024) 1–24

Contents lists available at ScienceDirect

ISPRS Journal of Photogrammetry and Remote Sensing

journal homepage: www.elsevier.com/locate/isprsjprs

# PROSAIL-Net: A transfer learning-based dual stream neural network to estimate leaf chlorophyll and leaf angle of crops from UAV hyperspectral images

Sourav Bhadra [a], Vasit Sagan [a,b,c,*], Supria Sarkar [a,c], Maxwell Braud [d], Todd C. Mockler [d], Andrea L. Eveland [d]

[a] Department of Earth & Atmospheric Sciences, Saint Louis University, Saint Louis, MO 63108, United States
[b] Department of Computer Science, Saint Louis University, Saint Louis, MO 63108, United States
[c] Taylor Geospatial Institute, Saint Louis, MO 63108, United States
[d] Donald Danforth Plant Science Center, Saint Louis, MO 63132, United States

ARTICLE INFO

*Keywords:*
Radiative transfer model
PROSAIL inversion
Artificial intelligence
Bi-directional reflectance distribution function
Plant phenotyping

ABSTRACT

Accurate and efficient estimation of crop biophysical traits, such as leaf chlorophyll concentrations (LCC) and average leaf angle (ALA), is an important bridge between intelligent crop breeding and precision agriculture. While Unmanned Aerial Vehicle (UAV)-based hyperspectral sensors and advanced machine learning models offer high-throughput solutions, collecting sufficient ground truth data for machine learning training can be challenging, leading to models that lack generalizability for practical uses. This study proposes a transfer learning based dual stream neural network (DSNN) called PROSAIL-Net, which leverages the knowledge gained from PROSAIL simulation and improves the estimation of corn LCC and ALA from UAV-borne hyperspectral images. In addition to hyperspectral data, the DSNN also includes solar-sensor geometry data, which was automatically extracted from a cross-grid UAV flight. The hyperspectral branch in the DSNN was also tested with multi-layer perceptron (MLP), long short-term memory (LSTM), gated recurrent unit (GRU), and 1D convolutional neural network (CNN) architectures. The results suggest that the 1D CNN architecture exhibits superior performance compared to MLP, LSTM, and GRU networks when used in the spectral branch of DSNN. PROSAIL-Net outperforms all other modeling scenarios in predicting LCC ($R^2$ 0.66, NRMSE 8.81%) and ALA ($R^2$ 0.57, NRMSE 24.32%) and the use of multi-angular UAV observations significantly improves the prediction accuracy of both LCC ($R^2$ improved from 0.52 to 0.66) and ALA ($R^2$ improved from 0.35 to 0.57). This study highlights the importance of utilizing large amounts of PROSAIL-simulated data in conjunction with transfer learning and multi-angular UAV observations in precision agriculture.

## 1. Background

Predicting leaf biophysical properties is crucial for sustainable agriculture as it allows for more efficient crop management. Leaf biophysical properties, such as chlorophyll content and leaf inclination angle, provide valuable information about the health and growth of crops, which can revolutionize the precision farming and crop breeding operations (Haboudane et al., 2002, Boggs et al., 2003, Mantilla-Perez and Fernandez, 2017). Chlorophyll is the pigment that allows plants to absorb light and convert it into energy through photosynthesis (Li, Sun, et al. 2019). Therefore, accurate measurement of leaf chlorophyll content (LCC) can reveal the health and vigor of a crop, as well as its ability to photosynthesize efficiently (Brewer et al., 2022, Vollmann et al., 2011). The leaf angle, also known as the leaf inclination angle or average leaf angle (ALA) in terms of the canopy, is the average angle at which most of the leaves in a canopy is held relative to the direction of light (Falster and Westoby, 2003). ALA can affect the amount of light that leaves receive and therefore has a direct impact on the photosynthesis and plant productivity as well as the planting densities (Falster and Westoby, 2003, Mantilla-Perez and Fernandez, 2017). Therefore, understanding the variability of LCC and ALA can help farmers in making more informed decisions about crop management, while the breeders can use

* Corresponding author at: Department of Earth & Atmospheric Sciences, Saint Louis University, Saint Louis, MO 63108, United States.
*E-mail address:* vasit.sagan@slu.edu (V. Sagan).

https://doi.org/10.1016/j.isprsjprs.2024.02.020
Received 11 May 2023; Received in revised form 22 February 2024; Accepted 23 February 2024
Available online 3 March 2024

the high-throughput data to create more efficient, resilient, and productive crop varieties.

Remote sensing technology, specifically the use of unmanned aerial vehicles (UAVs) has been revolutionizing crop biophysical trait estimation by providing a more efficient, cost-effective, and accurate way to collect data about crops (Xie and Yang, 2020, Burud et al., 2017). UAVs can be equipped with sensors that are enriched in higher spatial-spectral resolution and can cover large areas of land efficiently (Xiang and Tian, 2011, Colomina and Molina, 2014). Hyperspectral camera is one type of sensor that can accurately measure the reflectance or radiance of an object across a wide range of wavelengths (Barreto et al., 2019), ranging from visible (400–700 nm) to near-infrared (800–2500 nm). The UAV-borne hyperspectral camera can image the reflected light from the crops, which can be used to model different biophysical attributes. For example, chlorophyll in leaves absorbs sunlight in the blue and red regions for photosynthesis but reflects sunlight in the green and near-infrared region of the spectrum (Gitelson,Gritz,and Merzlyak, 2003). Alternatively, the amount of reflected light is lower when the leaves are perpendicular and rises with increasing ALA (Alton,North,and Los, 2007). However, the relationship between ALA and reflected spectra is complex and often relies on the leaf texture, wetness, and pigmentation (Blackburn, 1999, Grant,Daughtry,and Vanderbilt, 1993, Meng et al., 2014). With the ability to measure these biophysical traits non-destructively, UAV-borne hyperspectral cameras have greatly improved the precision of crop management and breeding (Zhang, Zhao, et al. 2019, Shu et al., 2021, Fan et al., 2022, Wang et al., 2023).

The UAV-based non-destructive measurement of crop biophysical attributes can be broadly divided into three different segments: 1) data-driven approach, 2) physics-based approach, and 3) hybrid approach. The data-driven approach or supervised machine learning uses statistical models trained on labeled data to predict different crop biophysical attributes from processed remote sensing data collected by the UAVs. Due to the simplicity and efficiency of many advanced machine learning models, data-driven approach is quite popular within the crop breeding and precision agriculture community. Numerous studies have explored partial least squares (Capolupo et al., 2015, Kanning et al., 2018), random forests (Lopez-Calderon et al., 2020, Peng et al., 2021), support vector regression (Yang et al., 2022, Wang et al. 2022, Singhal et al., 2019) and artificial neural networks (Borges et al., 2022, Maimaitijiang et al., 2020, Poblete et al., 2017) to estimate LCC or other traits from UAV-borne remote sensing products. Recent advancement in computer vision techniques, specifically convolutional neural networks (CNN) have enabled even more efficient data-driven learning as CNN can handle direct imagery as its inputs (Dericquebourg, Hafiane,and Canals, 2022, Bellis et al., 2022, Du et al., 2021, Zhang, Han, et al. 2019). However, the data-driven approaches often suffer from the challenges of requiring large ground truth datasets and reproducibility or robustness. Machine learning models have been often found to be more accurate and robust when large number of ground truth dataset is used in the training and validation (Kamilaris and Prenafeta-Boldu, 2018, Ruß and Brenning, 2010). This is especially evident in deep learning models, where a wealth of training data enables the model to expand its understanding and effectively make predictions for new, unseen data (Kamilaris and Prenafeta-Boldú, 2018, Moazzam et al., 2019). The collection of a substantial training dataset, which comprises both ground truths and aerial observations in an agricultural setting, can be a time-intensive, destructive, and costly process. (Bhat and Huang, 2021, Koh,Spangenberg,and Kant, 2021). Additionally, a machine learning model trained using datasets from one location, might not perform accurately for a different location where the interaction between genotypes, environment and management could be different (Paudel et al., 2021). Therefore, data-driven approaches are not entirely reliable for production-level decision making and require human-in-the-loop maintenance (Wu et al., 2022, Mosqueira-Rey et al., 2022).

Physics-based approach on the other hand, utilizes the inversion of radiative transfer model (RTM)-based simulation to estimate different crop biophysical attributes. RTMs are developed by the principles of radiative transfer, which is the study of how sunlight interacts with gases, particles, vegetation canopies and other objects in the environment (Hedley, Roelfsema, and Phinn, 2009). Since RTMs understand the spectral response relative to different object characteristics, scientists have explored the inversion of RTMs with remote sensing methods to reverse-engineer a certain trait (Yang et al., 2011, Pragnere et al., 1999). For crop biophysical trait estimation, PROSAIL is one of the most popular RTMs as it combines Leaf Optical Properties Database Model (PROSPECT-D) and Semi-Analytical Model of Inversion of Leaf reflectance (SAIL) together. PROSPECT-D describes the reflection and transmission of light by the leaves, while SAIL describes the radiative transfer in a vegetation canopy. Therefore, PROSAIL can take several leaf and canopy level attributes as inputs (such as, LCC, carotenoid, anthocyanin, leaf area index, leaf inclination angle, etc.) and outputs a reflectance spectra ranging from 400 nm to 2400 nm. Numerous studies have utilized the simulated spectra produced by randomly initializing PROSAIL variables and hyperspectral reflectance spectra from remote sensing techniques to explore the inverse relationship for estimating crop biophysical traits (Liang et al., 2015, Duan et al., 2014, Botha et al., 2007, Kayad et al., 2022, Casa and Jones, 2004, Liang et al., 2016). Most of these studies used look-up table or iterative optimization models (Baret and Buis, 2008) to estimate LCC and leaf area index parameters from crops. The major advantage of PROSAIL inversion over data-driven approach is the reproducibility or robustness of the models, as the PROSAIL simulation considers the biophysical characteristics of a crop given certain environmental conditions (Sun et al., 2022). However, the challenge of PROSAIL inversion is its 'ill-posed' problem, where different combinations of model parameters may contribute to similar canopy reflectance resulting in higher uncertainty (Combal, Baret, and Weiss, 2002, Li and Wang, 2011, Combal et al., 2003). Additionally, the inversion model can become too expensive to train as there can be millions of parameter combinations during the simulation (Liang et al., 2016).

Hybrid approach aims to combine the machine learning model and PROSAIL simulation model together in conjunction with hyperspectral observation. Such integration has the capabilities of reducing the model training time by leveraging the optimization efficiency of machine learning algorithms (de Sá et al., 2021). Many studies have integrated gaussian process (Camps-Valls et al., 2018, Svendsen et al., 2018), random forest (Campos-Taberner et al., 2018), support vector machine (Tuia et al., 2011) and artificial neural networks (Annala et al., 2020) with PROSAIL simulation and found considerable accuracy in prediction performance. However, the literature has not yet extensively explored the hybrid approach for crop biophysical attribute estimation with most studies focusing on satellite-based inversion, which doesn't provide the level of detail needed by crop breeders and precision agriculture practitioners. Therefore, there exists a knowledge gap in understanding the hybridization of PROSAIL and machine learning models to estimate different crop biophysical properties at plot-level from UAV-borne hyperspectral data.

Several studies have demonstrated the efficacy of hybrid models in predicting crop biophysical properties from UAV data. Many of them relied on multispectral sensors mounted in UAV, which typically involves blue, green, red, near-infrared and often red-edge region of the spectrum. Most of these studies utilized different types of inversion techniques in retrieving crop parameters from PROSAIL. For example, Wan et al. (2021) and Su et al. (2019) performed the inversion of CHL and LAI using the root mean squared error as the loss function between the simulated and observed response variables. Similarly, Antonucci et al. (2023) retrieved LCC, canopy chlorophyll, and LAI using the inversion of gaussian process regression. On the other hand, Sun et al. (2021) utilized the NDVI derived from the UAV multispectral camera as a correction parameter for the inverting the LAI from PROSAIL simulation and achieved improved result. However, the use of only 4 or 5 wavelengths during the PROSAIL inversion incurs the challenge of ill-

posed problem and might not be ideal to develop a generalized model for future use. Alternatively, few studies have explored the capabilities of hyperspectral data in PROSAIL simulation, where most of them employed the lookup table method to estimate either LAI or CHL for maize (Duan et al., 2014, Kayad et al., 2022), Gingko (Yin et al., 2022), rice (Wang et al., 2021), potato and sunflower (Duan et al., 2014). A lookup table is a well-organized collection of relationships, which is often limited by the size of the database and can be computationally intensive to use. Among these studies, Yin et al. (2022) determined the distributions of pigment content in Gingko plantations by leveraging both LiDAR (Light Detection and Ranging) and hyperspectral sensor along with PROSAIL inversion. Although they highlighted the superiority of coupling LiDAR and hyperspectral data with PROSAIL simulation, it is not always feasible to employ a co-aligned dual-sensor system for data collection and the postprocessing steps can be computationally expensive. Alternatively, Roosjen et al. (2018) employed a cost function optimization algorithm to estimate LAI and CHL of potato crop. Their approach introduced the concept of multi-angular spectral data in the process, which significantly improved the estimation accuracy. Recently, Zhang et al. (2021) used the concept of transfer learning in their deep neural network developed from PROSAIL-simulation to estimate CHL of winter wheat. Transfer learning enabled the reproducibility of knowledge learned by PROSAIL simulation to observed hyperspectral data collected by UAV. However, the study did not delve into the evaluation of various neural network structures and did not incorporate multi-angular observations into the analysis.

PROSAIL includes a set of solar-sensor angular information during the simulation, which is used to better understand the anisotropic relationship between the canopy spectral reflectance and its biophysical traits (Breunig et al., 2015). The angle of incoming solar radiation and reflectance can strongly interact with vegetation at both leaf (Jacquemoud and Baret, 1990) and canopy (Verhoef, 1984) level, which offer valuable information about the object. Therefore, several studies have achieved significant improvement in crop biophysical attribute estimation when multiple solar-sensor angles were considered during the hyperspectral data collection (Dorigo, 2012, Hilker et al., 2011, Song et al., 2016, Yang et al., 2011). However, collecting spectral data from multiple angles is often limited to handheld spectraradiometer (Thorp et al., 2015), goniometer (Sandmeier et al., 1998, Sandmeier, 2000), or satellite-borne hyperspectral imagers (Barnsley et al., 2004), which are challenging in a high-throughput phenotyping environment. For example, handheld spectraradiometer and goniometers (i.e., an instrument that can precisely measure the sensor geometry angles during data collection) can be accurate and precise but increases the logistical complexity. Satellite-based hyperspectral imagers on the other hand, cannot provide information at finer-scale, which is often required for crop breeding and precision agriculture practices. Therefore, UAVs mounted with hyperspectral sensors can offer better ground sampling distance to retrieve plant parameters and can be programmed to collect multi-angular observation. Although few studies have explored the use of multi-angular observation from UAV-borne hyperspectral sensors, they either explored only the anisotropic characteristics of plants (Burkart et al., 2015, Roosjen et al., 2017, Roosjen et al., 2016) or did not explore the use of efficient modeling techniques to perform PROSAIL inversion (Roosjen et al., 2018).

Deep neural networks (DNN) have improved the crop biophysical trait estimation accuracy from hyperspectral data by leveraging the complex non-linear relationship between traits and reflectance. Studies have utilized artificial neural network (ANN) or multi-layer perceptron (MLP) to estimate different crop traits and received comparable performance (Moghimi, Yang, and Anderson, 2020, Rehman et al., 2020, Feng et al., 2022, Fei et al., 2022). However, few studies have also explored into recurrent neural networks (RNN) and convolutional neural networks (CNN) for 1D spectral data and found better model performance. RNN was initially designed for handling sequence data as its input, specifically for natural language processing and timeseries forecasting (Michel, 2003). However, several studies have utilized the two most common types of RNN units, i.e., long short-term memory (LSTM) and gated recurrent unit (GRU), to understand the sequential pattern of hyperspectral data and received improved accuracy (Mou, Ghamisi, and Zhu, 2017, Paoletti et al., 2020, Hang et al., 2019). Alternatively, CNN has revolutionized the computer vision domain by extracting meaningful information from 2D images. However, CNN can be also extended to understand the 1D pattern from a signal data by considering a single dimensional kernel in the process. Many studies have reported the superior performance of 1D CNN architectures in extracting meaningful information from hyperspectral reflectance data (Huang, He, et al. 2022, Li et al., 2021, Mansuri et al., 2022, Riese and Keller, 2019, Liu and Xiao, 2020). However, none of these DNN architectures (other than the MLP) have not been well explored in terms of PROSAIL-inversion technique.

Transfer learning is a machine learning technique where a model trained on one task is fine-tuned for another similar task with limited training data (Pan and Yang, 2010). This approach has the potential to address one of the main challenges in using DNNs for crop biophysical trait estimation, which typically suffers from the unavailability of large datasets. By training a base model on a vast database of spectral data and corresponding crop traits generated from PROSAIL simulations, the PROSAIL-trained model can then be applied to UAV-borne hyperspectral data. The incorporation of varying solar-sensor geometry in the analysis can further increase the robustness of the model. Considering these facts, we propose a dual stream neural network (DSNN) approach that combines both solar-sensor geometry data and spectral data. This strategy is also aimed at leveraging transfer learning from PROSAIL to improve the prediction accuracy of LCC and ALA of maize crops. Therefore, we ask the following research questions in this study: 1) What type of DNN architecture (i.e., MLP, LSTM, GRU, or CNN) in the spectral stream of PROSAIL-Net is suitable for accurately estimating LCC and ALA? 2) How well the PROSAIL-Net perform compared to statistical machine learning algorithms in terms of prediction accuracy? 3) Does the inclusion of multi-angular UAV observations in the PROSAIL-Net provide better performance over single observations?

## 2. Experimental setup

### 2.1. Study area

Our study area is located in the heart of the USA Midwest, which produces over 33 % of the world's corn (Wang et al., 2020). Two locations were chosen for our experiment, i.e., two fields in Missouri and another one in Illinois. The Missouri (MO) sites were located at the Planthaven Farms, O'Fallon, where two experimental fields named D3 and D16 were prepared in 2021 and 2022, respectively. Another field named U1 was located at the University of Illinois in Urbana Champaign, Illinois (IL) in 2022. Both sites were planted with corn as part of the experimental design. The sites in O'Fallon, MO has an average yearly temperature of 14 °C with the hottest temperature in July (average 27 °C). It receives around 4 cm of precipitation on average each year with 65 % humidity. On the other hand, the IL site usually shows 11 °C yearly temperature on average, whereas the mean precipitation is around 3.7 cm over the year with 73 % humidity. The fields at these experimental sites were established as part of the research efforts between Saint Louis University, University of Illinois and Donald Danforth Plant Science Center.

### 2.2. Field design

The D3 field (Fig. 1a) was planted with 55 genotypes of corn on May 25, 2021. The lines were selected based on previous unpublished leaf angle and tassel branch number data. Additionally, classical mutants with distinct leaf angle phenotypes were also selected. The field was roughly 110 m in length and 30 m in width. The field was planted with

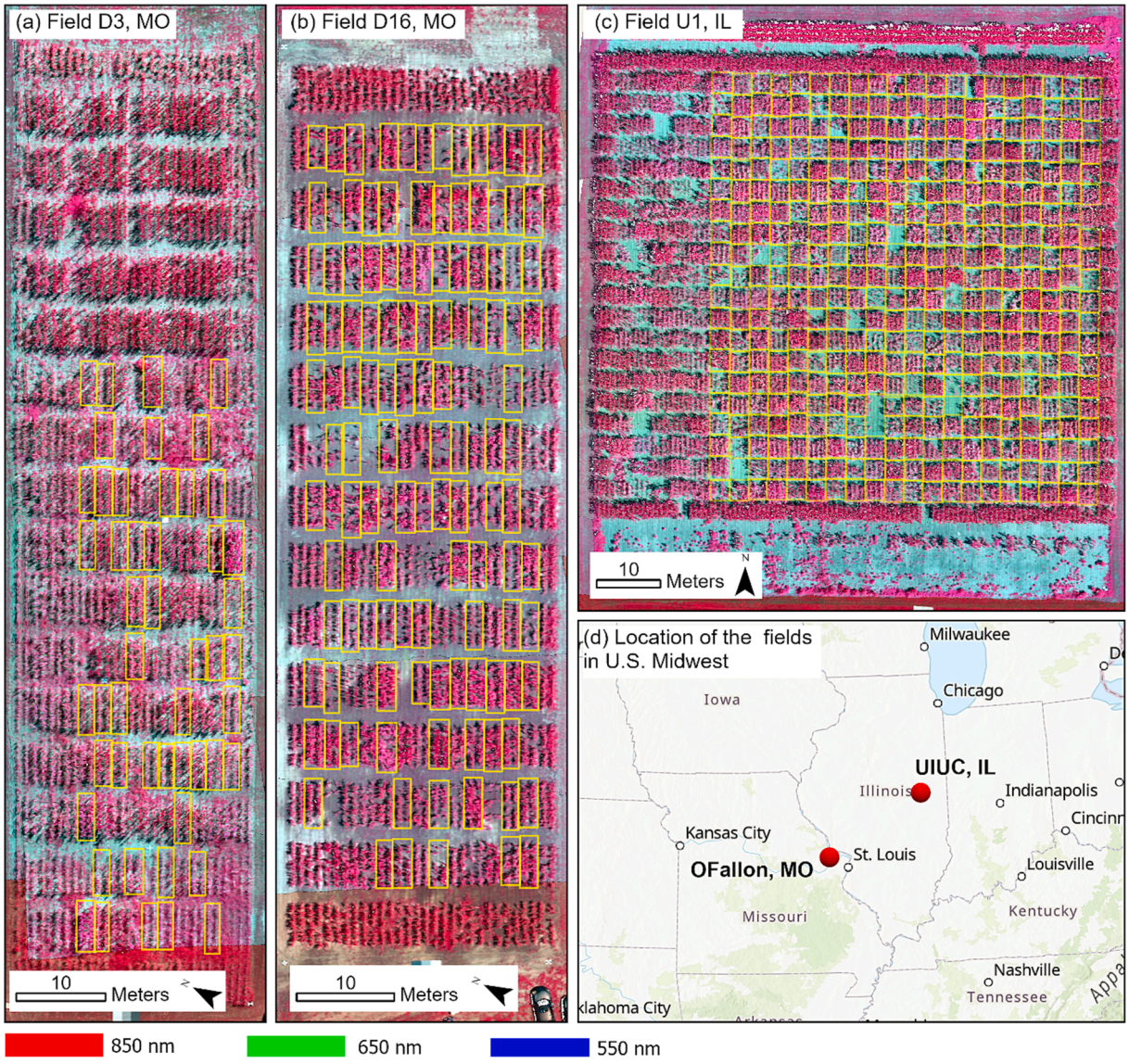


**Fig. 1.** Location of the study area. The D3 (a) and D16 (b) fields were located in O'Fallon, MO, whereas the U1 field (c) was in Champaign, IL. The sampling locations (i.e., plot boundaries) are marked with yellow polygons. Underneath each plot boundary, a false color composite (near infrared, red, and green bands) of the hyperspectral orthomosaic is shown. The false color composite shows slight difference of color intensity among plots. (For interpretation of the references to color in this figure legend, the reader is referred to the web version of this article.)

around 270 plots that contains two rows of corn. The plot dimension was roughly 5 m by 2 m and 2 replicates per genotype was considered. On the other hand, the D16 field (Fig. 1b) was planted on June 13, 2022, with 84 genotypes of corn. The field dimensions were also similar to D3 (i.e., 85 m in length and 30 m in width) that roughly contained 169 2-row plots of corn. For both D3 and D16, there were 2 replicates per genotype. However, not all the plots were considered part of the experiment (yellow boxes in Fig. 1 shows the plot boundary considered for phenotyping). Finally, the U1 field was larger than both D3 and D16. It was 90 m long but 80 m wide with around 385 (dimensions were 3 m by 3 m) 4-row plots of corn. Total 500 genotypes were planted on May 31, 2022, based on the same selection criteria we considered for D3 and D16.

## 3. Methods

### 3.1. Data collection

Two types of datasets were collected in this experiment, i.e., UAV-borne hyperspectral imagery and ground truth data from selected samples. The overall process and data collection scenario is illustrated in Fig. 2.

#### 3.1.1. UAV data collection

We used a DJI Matrice 600 Pro UAV platform (DJI, Shenzhen, China) equipped with a Headwall NanoHyperspec VNIR camera (Headwall Photonics, Massachusetts, USA). The M600 Pro is a popular UAV hexacopter, which has a maximum payload capacity of 6 kg. The NanoHyperspec hyperspectral camera was aligned with APX-15 Global Navigation System Satellite/Inertial Measurement (GNSS/IMU) unit (Applanix, Ontario, Canada) and the whole system was mounted with the UAV using a Ronin-MX gimbal (DJI, Shenzhen, China). The use of gimbal and high-resolution GNSS/IMU unit ensures good quality data collection specifically for a push-broom hyperspectral sensor. We also used a reflectance tarp (Fig. 2d) on the ground to perform radiometric calibration of the hyperspectral cubes after the data collection. The NanoHyperspec camera is a line scanner hyperspectral camera that has 12 mm focal length and can capture 640 spatial pixels perpendicular to

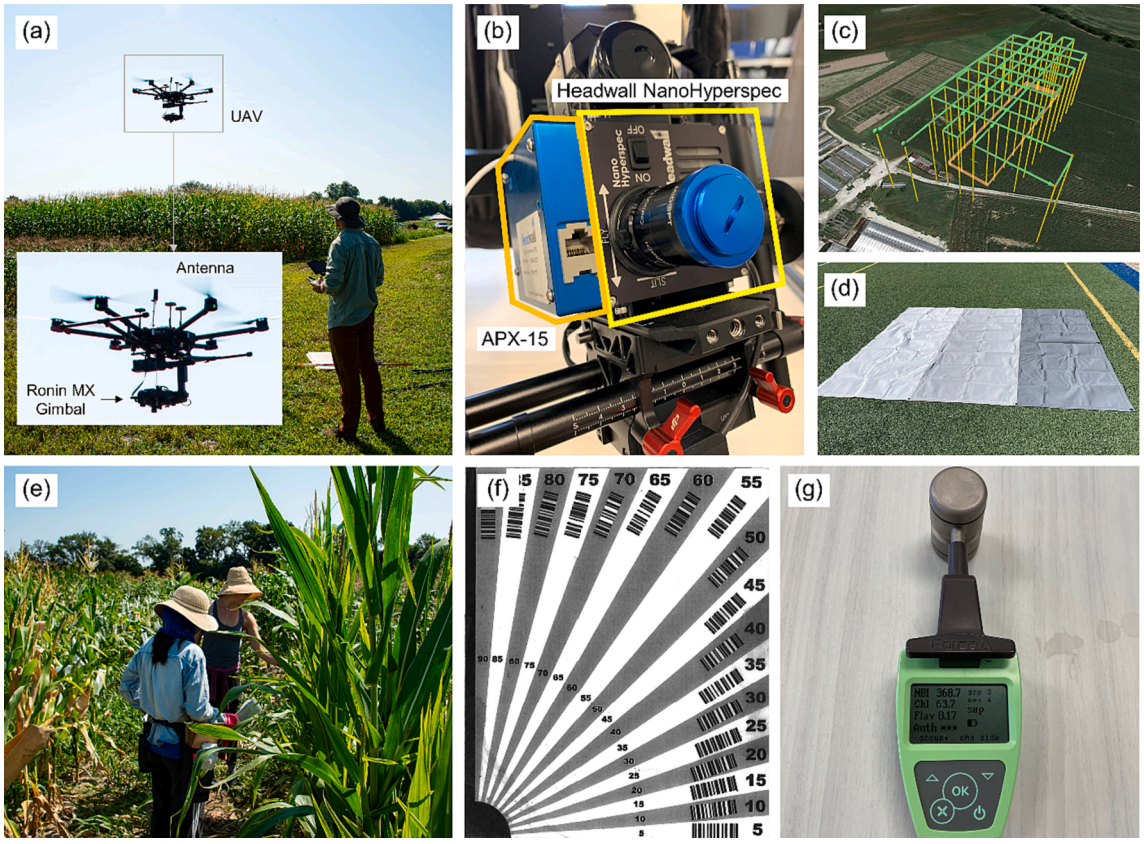


**Fig. 2.** Data collection scenarios. The UAV system (a) consisted of a gimbal that holds the hyperspectral sensor and GNSS/IMU (b). The UAV was flown in a cross-grid fashion (c) using the UGCS software. The radiometric calibration was done using a reflectance tarp (d) laid down on the ground during data collection. The ground truth data collection was performed on the same days of the UAV flights by manual measurement(e). We calculated the ALA using a handmade protractor tool (f), which can calculate the angle between the stem and leaf, and LCC using a Dualex Scientific 4 instrument (g).

its flight path. Therefore, we had to define a geographic polygon boundary during the data collection window, and the system automatically started capturing data whenever the UAV system was inside that boundary. The camera provided 269 spectral bands ranging from 400 nm to 1000 nm in very near-infrared (VNIR) region with around 2.3 nm spectral resolution. The flight missions were planned in a cross-grid pattern using the UGCS Mission Planning software (v4.14, SPH Engineering, Riga, Latvia). The flights had 50 m altitude, 3 m/s speed, which roughly gave us around 3 cm ground sampling distance (GSD) per pixel.

Total four UAV flights were conducted in the experimental sites. Table 1 shows the list of days for data collection. For each day, we chose to fly around noon or a little before noon to avoid unpredictable cloud conditions. The dates were chosen based on clear sky condition and maturity stages of the corn. We chose the early reproductive stages of corn as the data collection dates.

### 3.1.2. Ground truth data collection

The number of samples collected for LCC and ALA are provided in Table 1. We used a Dualex Scientific 4 (Force-A, Orsay, Ile-de-France, France) instrument to measure the LCC for each sample plot. Three well-lit healthy leaves from close to the top of the canopies were selected randomly for each plot. We used the average value of the three leaves as one representative LCC value. Ground truthing of leaf angle was performed using a simple printed protractor tool (Fig. 2f), measured as degrees from horizontal. The leaf directly above the highest ear was chosen, or if no ear was present, the fifth leaf from the top of the plant. Plants that didn't have an ear and had not yet tasseled were not measured. The stem of the plant was aligned to the protractor, and the angle of the leaf was measured to the closest 5°. Three replicates from each plot were measured, with 2 replicate plots. However, the PROSAIL simulation only considers the leaf inclination angle, which refers to the angle at which a leaf is tilted relative to the direction perpendicular to the ground. Since the stalk of corn plant is commonly perpendicular to the ground, we subtracted the leaf angle measured using the protractor tool from 90° to get the leaf inclination angle for PROSAIL. The average value of all three replicates within a plot was considered as the ALA for this study.

**Table 1**
Data collection dates and number of ground truth samples.

| Date | Field Name | Number of Ground Truth Samples | |
|---|---|---|---|
| | | LCC | ALA |
| July 20, 2021 | D3 | 50 | 50 |
| August 4, 2021 | D3 | 50 | 50 |
| August 11, 2022 | D16 | 100 | 116 |
| August 17, 2022 | U1 | 0 | 385 |
| Total Samples | | 200 | 601 |

## 3.2. PROSAIL-Net schematics

### 3.2.1. PROSAIL simulation

PROSAIL is a radiative transfer model (RTM) that combines PROSPECT-D and SAIL together (Fig. 3a). PROSPECT-D is a leaf model which understands different leaf biophysical properties (Table 2) and simulates leaf reflectance and transmittance. The SAIL model on the other hand takes the leaf reflectance and transmittance from the PROSPECT-D model along with several canopy, soil and viewing geometry parameters to simulate canopy reflectance. The canopy reflectance ranges from 400 nm to 2500 nm with 1 nm interval (Fig. 3c).

For the simulation part, we first identified typical ranges of different

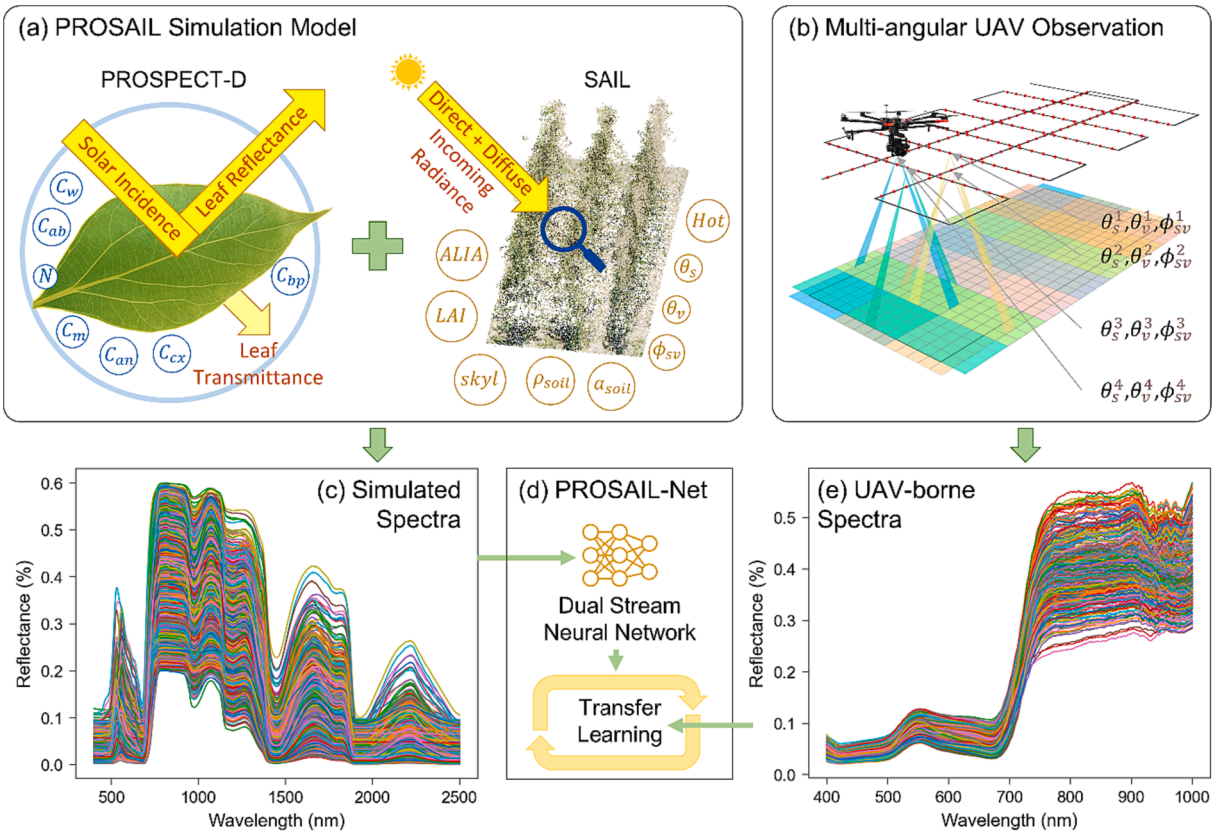


**Fig. 3.** The schematics of PROSAIL-Net. The PROSAIL simulation (a) is consisted of PROSPECT-D, a leaf model, and SAIL, a canopy model. The random initialization of PROSAIL variables results in a large number of simulated spectra (c). The multi-angular cross-grid UAV flight (b) enables us to get variable $\theta_s$, $\theta_v$, and $\phi_{sv}$, along with hyperspectral spectra (d). The PROSAIL-Net consists of a neural network trained by the simulated dataset and later trasnfering that knowledge to the observed data from UAV hyperspectral system.

**Table 2**
Overview of the PROSAIL input variables of corn based on literature review.

| Model | Variable Name | Symbol | Unit | Typical Range |
|---|---|---|---|---|
| PROSPECT-D (Leaf model) | Leaf structure index | $N$ | Unitless | 1.2 – 1.8 |
| | Chlorophyll $a$ + b content | $C_{ab}/LCC$ | $\mu g/cm^2$ | 0.1 – 80 |
| | Total carotenoid content | $C_{cx}$ | $\mu g/cm^2$ | 1.0 – 24.0 |
| | Total anthocyanin content | $C_{an}$ | $\mu g/cm^2$ | 1.2 – 1.8 |
| | Brown pigments | $C_{bp}$ | Unitless | 0.01 – 1.0 |
| | Dry matter content | $C_m$ | $g/cm^2$ | 0.004 – 0.0075 |
| | Leaf water depth | $C_w$ | $cm$ | 0.01 – 0.03 |
| SAIL (Canopy model) | Leaf area index | $LAI$ | $m^2/m^2$ | 0.1 – 7.0 |
| | Average leaf inclination angle | $ALA$ | (°) | 10.0 – 80.0 |
| | Hot spot parameter | $Hot$ | $m/m$ | 0.01 – 0.20 |
| | Soil reflectance | $\rho_{soil}$ | (%) | – |
| | Soil brightness factor | $\alpha_{soil}$ | Unitless | 1 |
| | Fraction of diffuse illumination | $skyl$ | (%) | 23 |
| | Solar zenith angle | $\theta_s$ | (°) | 10.0 – 90.0 |
| | Sensor (viewing) zenith angle | $\theta_v$ | (°) | 10.0 – 90.0 |
| | Relative azimuth angle between sun and sensor | $\phi_{sv}$ | (°) | 10.0 – 360.0 |

PROSPECT-D and SAIL variables available for corn in the literature (Bsaibes et al., 2009, Koetz et al., 2005, Kong et al., 2016, Berger et al., 2018). The ranges considered for our study is listed in Table 2. We used the PROSAIL bindings in Python developed by Domenzain, Gómez-Dans, and Lewis (2019). We simulated 100,000 simulated spectra using randomly assigned variables within the ranges of Table 2. However, we added some constraints during the simulation, which excluded the generation of unusual spectral data. For instance, some combination of angular variables may result in null spectral data, which were discarded automatically from the simulation. In addition, if the reflectance values were more than 1.0 or negative, such samples were dropped as well. The soil reflectance spectra were collected from 10 well sunlit spots randomly distributed within the experimental fields. We used the Spectral Evolution PSR-3500 handheld spectraradiometer to capture the reflectance spectra (400 – 2500 nm) from the soil for each day. The soil reflectance from 10 samples were then averaged together as the input for PROSAIL model. The solar zenith ($\theta_s$), sensor (or viewing) zenith ($\theta_v$), and relative azimuth angle between the sun and sensor ($\phi_{sv}$) were also considered since we hypothesized the influence of multi-angular viewpoint would have better performance accuracy in the inversion model.

### 3.2.2. Transfer learning

Transfer learning is a machine learning technique in which a model trained on one task (i.e., source domain) is re-purposed for a different task (i.e., target domain) to achieve robust performance (Pan and Yang, 2010). The goal of transfer learning is to leverage the knowledge learned from the source domain to improve the performance of the model on the target domain, especially when the amount of labeled data in the target domain is limited. There are different types of transfer learning, including inductive, transductive, and unsupervised transfer learning (Zhuang et al., 2021). In inductive transfer learning, the pre-trained model is used as a feature extractor for a new model that is trained on the target domain. In transductive transfer learning, the pre-trained

model is fine-tuned on the target domain using a limited set of labeled data, and in unsupervised transfer learning, the pre-trained model is used as a starting point for training a new model on the target domain without using labeled data. Based on the scenario of our problem, it falls under the transductive transfer learning. However, our source domain is the PROSAIL simulation model (Fig. 3c) and multi-angular UAV data (Fig. 3b), where the features are the spectral data and solar-sensor geometry data. The target domain for our case is also the spectral data from UAV-borne hyperspectral sensor and the solar-sensor geometry data extracted from the GNSS/IMU of the UAV. Therefore, the transfer learning scenario is straightforward, and the features of source domain and target domain are the same. This is also known as "fine-tuning" transfer learning (Vrbančič and Podgorelec, 2020) as the task is to leverage the large training dataset of the source domain into the small amount of labeled data in the target domain.

The basis of our PROSAIL-Net was simply three-fold, i.e., first, simulate a large amount of spectral data from PROSAIL using many combinations of the crop biophysical variables specified in Table 2; second, train two base neural networks from the simulation data where the inputs are spectral and solar-sensor geometry data, and the output is either LCC or ALA; and finally, use the pretrained base model that performed the best to estimate LCC or ALA from observed UAV data.

Our initial analysis of PROSAIL-simulated and UAV-extracted spectral data revealed that the UAV spectra includes some noise within its value. The noise can originate from various factors, such as, atmospheric environment, UAV flying platform, imaging optical devices, etc. (Kedzierski et al., 2019, Sekrecka, Wierzbicki, and Kedzierski, 2020, Arroyo-Mora et al., 2021). Consequently, we applied the Savitzky-Golay transform (Press and Teukolsky, 1990), a frequently utilized smoothing method for spectral data, to process the UAV spectra with the objective of eliminating noise. The method involves fitting a polynomial function to a window of adjacent data points and then using the polynomial to estimate the smooth values of the data points within the window. The transformation can be expressed by Equation (1):

$$\hat{y}_i = \sum_{j=-m}^{j=m} c_j * y_{i+j} \tag{1}$$

where, $\hat{y}_i$ is the estimated smoot value of the data point at position $i$, $y_{i+j}$ are the data points within the window centered at $i$, $m$ is the half-width

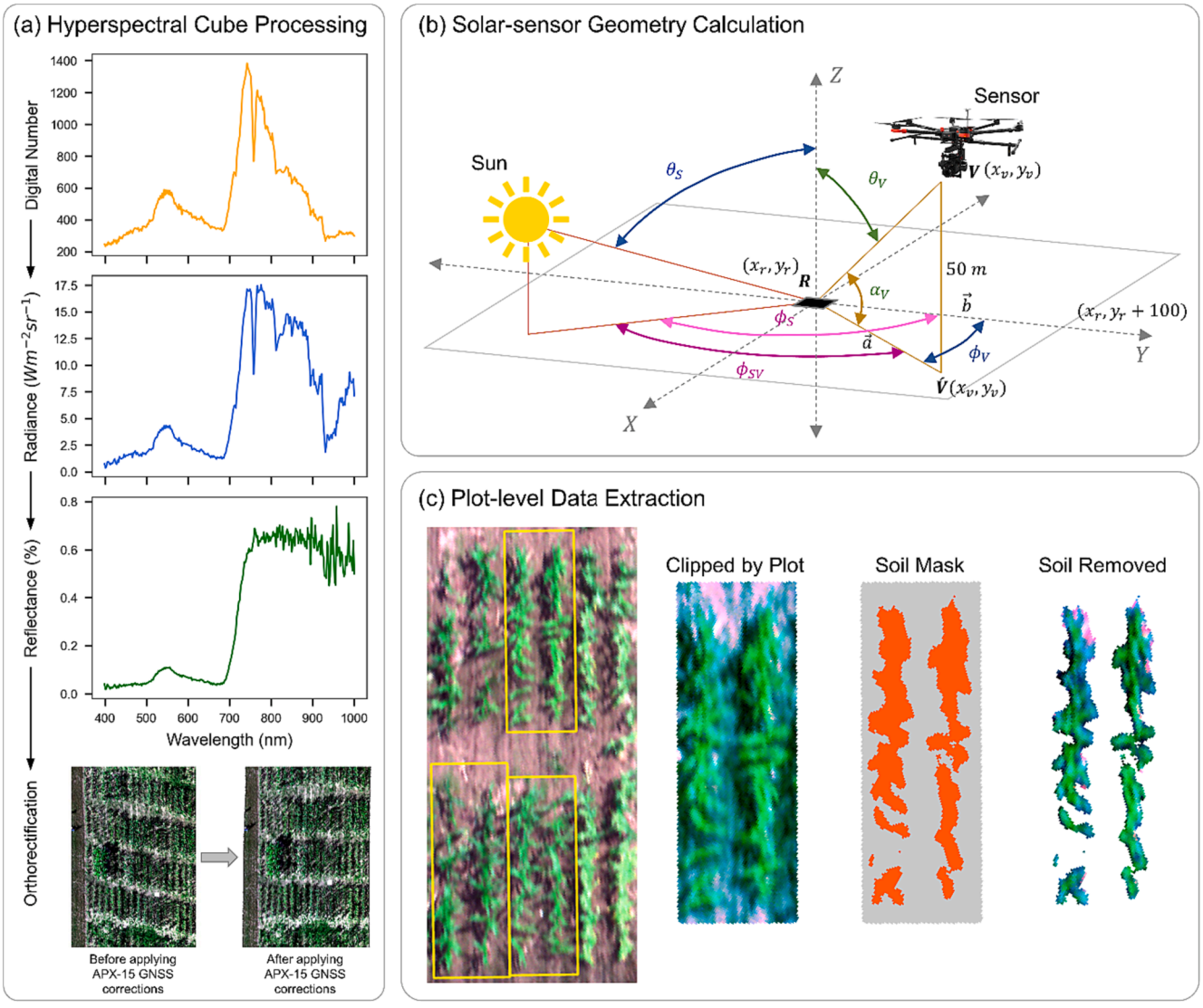


**Fig. 4.** Data processing steps. The hyperspectral cubes were first converted from digital number to radiance to reflectance to orthorectified rasters (a). The solar-sensor geometry was calculated for each hyperspectral cube using the methods described in Bhadra et al. (2022). Figure (b) was updated with permissions from the authors of Bhadra et al. (2022). Finally, the plot-level data extraction (c) was done using a custom-made Python tool that clips the data based on plot boundary, applies k-nearest neighbor to get soil mask, and extracts the soil removed average hyperspectral spectra per plot.

of the window, and $c_j$ are the coefficients of the polynomial function, which are calculated using a least-squares method. We use a 1st order polynomial and a window length of 13 for the Savitzky-Golay transform, which gave us an optimum spectrum from UAV that closely matches the PROSAIL spectra. The details of PROSAIL-Net neural network structure are explained in Section 3.4.

### 3.3. Data preprocessing

The data preprocessing steps can be broadly categorized into: a) hyperspectral cube processing, b) solar-sensor geometry calculation, and c) plot-level data extraction. Fig. 4 illustrates the major steps involved in each category.

#### 3.3.1. Hyperspectral cube processing

The hyperspectral images were collected as 3D cubes across the flight path, where the $x$ and $y$ axis represent the spatial dimension, and the $z$ axis holds the spectral information. The initial data cube only stored the amount of light passing through the sensor as Digital Numbers (DN). We used Headwall's proprietary software, 'Spectral Viewer', to convert the DN values into radiance ($Wm^{-2}sr^{-1}$), which is the amount of light energy reflected by an object. The conversion is done using the empirical line method which is a linear regression model that is trained for each sensor to convert raw DN into radiance values. Each unique sensor comes with its own proprietary model within the software for this conversion. To account for the variability of solar irradiance or solar intensity during the data collection, we converted the radiance into reflectance values by using a reflectance tarp placed on the ground during data collection (Fig. 2d). The reflectance tarp has three different levels, i.e., 56 %, 33 % and 11 %, among which we chose the 56 % for reflectance calculation based on the recommendation from Headwall (Barreto et al., 2019). Finally, the hyperspectral cubes were geometrically corrected using the onboard APX-15 GNSS/IMU data and photogrammetric calibration procedures available in the Spectral Viewer software. Fig. 4a shows the major steps taken into consideration for the hyperspectral data cube processing part.

#### 3.3.2. Solar-sensor angle calculation

The solar and sensor geometry corresponding to each hyperspectral cube were calculated based on the methodologies developed by Bhadra et al. (2022). The pipeline can take in different cube and corresponding GNSS/IMU information as inputs while resulting three geospatial rasters of solar zenith angle ($\theta_s$), sensor zenith angle ($\theta_v$), and relative azimuth angles ($\phi_{sv}$).

The solar zenith ($\theta_s$) and azimuth ($\phi_s$) angles were calculated using the PVLIB library (v0.9.0), which is an astronomical library in Python (Holmgren, Hansen, and Mikofski, 2018). $\theta_s$ is a function of time, latitude, and longitude information, which can be extracted from the GNSS/IMU device with the functionalities developed by Bhadra et al. (2022). On the other hand, $\phi_s$ depends on the time and latitude of the corresponding pixel and was calculated directly by PVLIB. Both $\theta_s$ and $\phi_s$ were calculated for each pixel of each hyperspectral cube, and later converted as a geospatial raster data for input in the PROSAIL model.

Alternatively, the sensor zenith ($\theta_v$) and azimuth ($\phi_v$) angles were calculated using trigonometric functions. Since the local coordinates of sensor location, $V(x_v, y_v)$ and corresponding pixel location, $R(x_r, y_r)$, can be known through the Universal Transverse Mercator (UTM) projection system, and the flight altitude was always 50 m, we can calculate $\alpha_v$ as Equation (2) and then $\theta_v$ with Equation (3). The $\phi_v$ was calculated using equation (4), where the $\vec{a}$ is the true north vector and $\vec{a}$ is the vector between $V$ and $R$. Finally, the relative azimuth angle between sensor and sun can be calculated using Equation (5).

$$\alpha_v = tan^{-1}\frac{50}{\sqrt{(x_v - x_r)^2 + (y_v - y_r)^2}} \tag{2}$$

$$\theta_v = 90^o - \alpha_v \tag{3}$$

$$\phi_v = \cos^{-1}\left[\frac{\vec{a} \bullet \vec{b}}{|\vec{a}|\left|\vec{b}\right|}\right] \tag{4}$$

$$\phi_{sv} = \phi_s - \phi_v \tag{5}$$

The angles were first calculated based on the pixel coordinates of each hyperspectral cube. For further use as the input in the PROSAIL model, $\theta_s$, $\theta_v$, and $\phi_{sv}$ were converted as a geospatial raster data.

#### 3.3.3. Plot-level data extraction

The plot boundaries were digitized in ArcGIS Pro using polygons. Then, plot-level average reflectance values for each wavelength were extracted using an automated pipeline developed in Python. We used geopandas, rasterio, and other GDAL-based open-source geospatial libraries to read the hyperspectral cube, remove soil pixels and then calculate mean spectral data. The soil pixels were identified for each vegetation cube by employing k-means clustering algorithm with 2 clusters. Since the plot-level data was extracted for individual hyperspectral cubes, there were instances where the plot boundary only covered a small portion of vegetation. Those cases were identified by using a threshold for the ratio of pixel area in that cube and the corresponding plot area. The overall process is illustrated in Fig. 4c.

### 3.4. Dual stream deep neural network

The PROSAIL-Net was built as a dual-stream deep neural network (Fig. 5a) since it has to handle two types of input dataset (i.e., angle and spectra data) within its architecture. We decided to use a simple multilayer perceptron (MLP) network for the angel branch and experimented with different types of neural networks for the spectra branch. Finally, the outputs from both branches were concatenated together using a concatenation layer followed by the prediction layer of LCC and ALA.

#### 3.4.1. Solar-sensor angle branch

The angle branch consists of three features as its inputs, i.e., solar zenith angle $\theta_s$, sensor zenith angle $\theta_v$ and relative azimuth angle ($\phi_{sv}$), followed by a MLP network. MLP is composed of multiple layers of artificial neurons. The neurons in each layer are connected to the neurons in the next layer through a set of weights, and the network is trained to adjust these weights to perform a regression task. Each neuron in the MLP perform the following equation:

$$y = f(W \cdot x + b) \tag{6}$$

where, $y$ is the output of the network, $f$ is the activation function, $W$ is the weight matrix, $b$ is the vias vector, $x$ is the input, and $\cdot$ is the dot operator. The MLP network we designed for this branch includes four hidden dense layers with 2, 8, 16, and 32 neurons, respectively. Each layer was accompanied by a Rectified Linear Unit (ReLU) activation function.

#### 3.4.2. Spectral branch

The spectra branch was tested with several types of neural networks, i.e., MLP, convolutional neural network (CNN), long short-term memory (LSTM), and gated recurrent unit (GRU).

*3.4.2.1. Multi-layer perceptron.* The MLP network used in the spectra branch was similar to the one in angle branch. However, since the spectra data had 269 features as its input, we increased the number of hidden layers along with the number of neurons in each layer (Fig. 5b). We also introduced some dropout layers in between each block of layers to reduce potential overfitting issues.

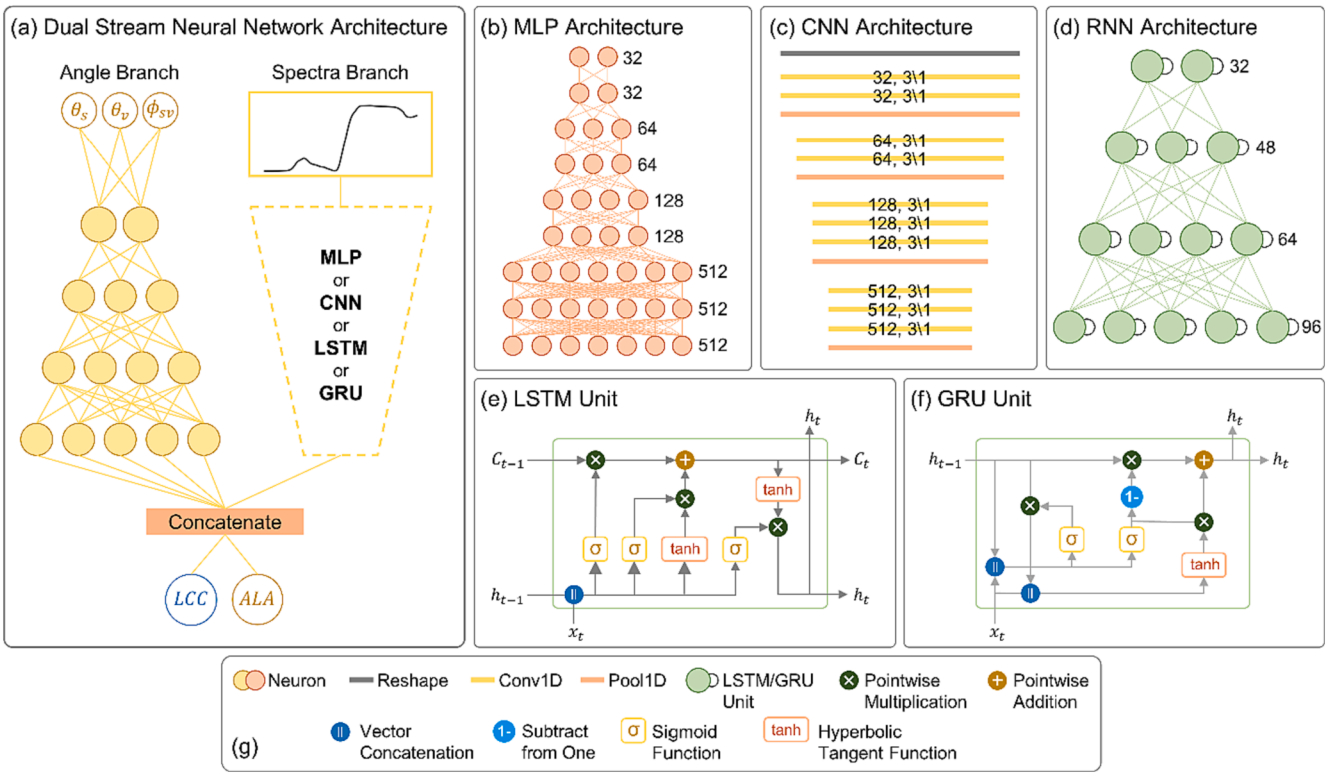


**Fig. 5.** The schematics of dual stream neural network (a) where the angle branch uses a simple MLP to process the solar-sensor geometry data, and the spectra branch deals with the hyperspectral data using either MLP (b), CNN (c) or RNN (d) architectures. Two types of RNN units were considered, i.e., LSTM (e) and GRU (f). The explanation of different icons are given below as legends. The information from both angle branch and spectra branch was concatenated together and finally an output layer was used to predict either LCC or ALA.

*3.4.2.2. Long short-term memory.* Long short-term memory (LSTM) is a type of recurrent neural networks (RNNs) that are designed to handle sequential data, such as, natural language, time series or signal data. They can maintain a memory of previous inputs and use that information to inform the current output. A LSTM unit (Fig. 5e) use three gates (i.e., input, forget, and output gates) to control the flow of information through the network (Equations (7) – (11)). The input gate ($i_t$) controls the flow of new information into the cell state, the forget gate ($f_t$) controls the flow of information out of the cell state, and the output gate ($o_t$) controls the flow of information from the cell state to the output. These gates are controlled by different weights and biases and are modeled by the following equations:

$$i_t = \sigma(W_i \cdot x_t + U_i \cdot h_{t-1} + b_i) \tag{7}$$

$$f_t = \sigma\left(W_f \cdot x_t + U_f \cdot h_{t-1} + b_f\right) \tag{8}$$

$$o_t = \sigma(W_o \cdot x_t + U_o \cdot h_{t-1} + b_o) \tag{9}$$

$$c_t = f_t * c_{t-1} + i_t * \tanh(W_c \cdot x_t + U_c \cdot h_{t-1} + b_c) \tag{10}$$

$$h_t = o_t * \tanh(c_t) \tag{11}$$

where, $x_t$, $h_t$, and $c_t$ are the input, hidden state, and cell state at time step $t$, respectively. In addition, the parameters $W$, $U$, and $b$ are the weights and biases of the gates, respectively. The LSTM architecture is illustrated in Fig. 5d, where four hidden layers of variable LSTM units were stacked together as the basis of the network.

*3.4.2.3. Gated recurrent unit.* Gated recurrent unit (GRU) is another type of RNN that can handle sequential data. It is similar to a LSTM in its functioning but has fewer parameters and is computationally more efficient. The GRU cell (Fig. 5f) has two gates, i.e., the update gate and the reset gate (Equations (12) – (14). The update gate ($z_t$) controls the amount of information to be kept from the previous hidden state and the current input, and the reset gate decides how much of the previous hidden state information should be forgotten.

$$z_t = \sigma(W_z \cdot x_t + U_z \cdot h_{t-1} + b_z) \tag{12}$$

$$r_t = \sigma(W_r \cdot x_t + U_r \cdot h_{t-1} + b_r) \tag{13}$$

$$h_t = (1 - z_t) * h_{t-1} + z_t * \tanh(W_h \cdot x_t + r_t * (U_h \cdot h_{t-1} + b_h)) \tag{14}$$

where, $x_t$, $z_t$, $r_t$ and $h_t$ are the input, update state, reset state, and hidden state at time step $t$, respectively, and $W$, $U$, and $b$ are the weights and biases of the gates. The GRU architecture is illustrated in Fig. 5d, where four hidden layers of GRU units were stacked together to process the sequential data.

*3.4.2.4. Convolutional neural network.* Convolutional neural network (CNN) is a highly popular method to extract meaningful features and patterns from 2D images. However, the concepts of 2D convolution can be extended to 1D convolution that can handle a 1D array as input. The 1D CNN is composed of multiple layers, each of which contains a set of convolutional and pooling filters that are trained to extract specific features from the input data. If $f$ is the input vector with length $n$ and $g$ is the kernel with length $m$, the convolution $f*g$ of $f$ and $g$ is defined as:

$$(f*g)(i) = \sum_{j=1}^{m} g(i) \bullet f\left(i - j + \frac{m}{2}\right) \tag{15}$$

The mathematical operation in Equation (15) slides a kernel over a 1D spectra and multiply the overlapping kernel with the spectra followed by the addition of them together. After each convolution layer or a block of convolution layers, we applied a 1D max pooling layer, which is also a sliding kernel moving through the spectra. In this case, the max

pooling layer takes the maximum value within the window and assign it as the output for that position. Max pooling helps reducing the high dimensionality in spectral data while retaining the most influential information within the data.

The 1D CNN architecture considered in this study was inspired by the skeleton of VGG architecture (Simonyan and Zisserman, 2015). VGG is one of most popular architecture for its strong performance, simplicity, standardization and for being one of the first architectures that used small convolutional filters and very deep architectures (Pak and Kim, 2017, Ajit,Acharya,and Samanta, 2020). We used four blocks of convolution and pooling layers, where each convolution has 32 to 512 kernels with $3 \times 1$ shape and pooling shape of $2 \times 1$ (Fig. 5b). At the end of the network, the feature maps were flattened to match the dimensions of the dense layer output of angle branch.

### 3.5. Statistical machine learning algorithms

We trained several statistical machine learning algorithms which has shown consistent performance in crop biophysical trait estimation from hyperspectral data. We chose partial least squares regression or PLSR (Foster, Kakani, and Mosali, 2017, Shen et al., 2020), random forest regression or RFR (Yang et al., 2021, Wang, Zhao, and Yin 2022), and support vector machine regression or SVR (Karimi et al., 2008, Huang et al., 2019) as the statistical machine learning algorithms due to their popularity and simplicity. For the statistical machine learning portion, we tested two types of training scenarios, i.e., a) ML-Raw and b) ML-VI. In the ML-Raw models, average reflectance from each plot for all the wavelengths (i.e., 269 bands) were used as the input. For the ML-VI models, vegetation indices (VIs) were calculated before feeding them into the models. Research has shown that VIs can minimize the effects of illumination condition, solar angle and enhance the contrast between soil and vegetation (Fang and Liang, 2014, Lambin, 2001). Table 3 shows a list of the VIs considered for this analysis.

### 3.6. Model training and evaluation

The model training scenarios in this study can be categorized into two different sections, i.e., a) statistical machine learning and b) deep learning. In this section, we will explain how different models were trained to estimate LCC and ALA. The total dataset was randomly split into two sets, i.e., training (70 %) and testing (30 %) set. The models were trained using the train set, whereas the evaluation was performed with the test set that was not seen by the models during training.

#### 3.6.1. Training statistical machine learning algorithms

The statistical machine learning algorithms (i.e., PLSR, RFR and SVR) for two modeling scenarios (i.e., ML-Raw and ML-VI) were trained using the Scikit-learn package (v1.0.1) in Python. Hyperparameter tuning is critical for optimizing the performance of statistical machine learning algorithms as it involves selecting the values of parameters that govern the learning process. The optimal values of hyperparameters can be determined through a systematic search over the parameter space, which can result in a significant improvement in the accuracy of the model (Dewi and Chen, 2019, Liu, Wu, and Chen 2020). We used the grid search hyperparameter tuning, which is a method of systematically searching over a predefined hyperparameter space in order to determine

**Table 3**
List of VIs used in ML-VI modeling, where in $\rho_n$, $\rho$ is the reflectance of wavelength $n$.

| VI | Abbreviation | Formula | Reference |
|---|---|---|---|
| ARI | Anthocyanin Reflectance Index | $\frac{1}{\rho_{550}} - \frac{1}{\rho_{700}}$ | Gitelson, Merzlyak, and Chivkunova (2001) |
| NDVI | Normalized Difference Vegetation Index | $\frac{\rho_{860} - \rho_{650}}{\rho_{860} + \rho_{650}}$ | Rouse et al. (1974) |
| NDRE | Normalized Difference Red-edge Index | $\frac{\rho_{860} - \rho_{720}}{\rho_{860} + \rho_{720}}$ | Nichol et al. (2000) |
| GNDVI | Green Normalized Vegetation Index | $\frac{\rho_{860} - \rho_{560}}{\rho_{860} + \rho_{560}}$ | Gitelson et al. (1996) |
| GDVI | Green Difference Vegetation Index | $\rho_{860} - \rho_{560}$ | Tucker et al. (1979) |
| ARVI | Atmospherically Resistant Vegetation Index | $\frac{\rho_{800} - [\rho_{680} - \rho_{450} + \rho_{680}]}{\rho_{800} + [\rho_{680} - \rho_{450} + \rho_{680}]}$ | Kaufman and Tanre (1992) |
| CCCI | Canopy Chlorophyll Content Index | $\frac{\rho_{800} - \rho_{715}}{\rho_{800} + \rho_{715}} / \frac{\rho_{800} - \rho_{680}}{\rho_{800} + \rho_{680}}$ | Barnes et al. (2000) |
| CARI | Chlorophyll Absorption Ratio Index | $\frac{\rho_{700}}{\rho_{670}} * [(\rho_{700} - \rho_{670}) - 0.2(\rho_{700} - \rho_{550})]$ | Daughtry et al. (2000) |
| GCI | Green Chlorophyll Index | $\frac{\rho_{800}}{\rho_{560}} - 1$ | Hunt et al. (2011) |
| RECI | Red Edge Chlorophyll Index | $\frac{\rho_{800}}{\rho_{715}} - 1$ | Gitelson, Keydan, and Merzlyak (2006) |
| CI | Curvature Index | $\frac{\rho_{675} * \rho_{690}}{\rho_{683}^2}$ | Zarco-Tejada et al. (2001) |
| Datt1 | Datt Index 1 | $\frac{\rho_{850} - \rho_{710}}{\rho_{850} - \rho_{680}}$ | Datt (1999) |
| Datt3 | Datt Index 3 | $\frac{\rho_{754}}{\rho_{704}}$ | Datt (1999) |
| Datt4 | Datt Index 4 | $\frac{\rho_{672}}{\rho_{530} - \rho_{708}}$ | Datt (1999) |
| Datt6 | Datt Index 6 | $\frac{\rho_{860}}{\rho_{550} - \rho_{708}}$ | Datt (1999) |
| EVI | Enhanced Vegetation Index | $2.5 * \frac{\rho_{860} - \rho_{650}}{\rho_{860} + 6 * \rho_{650} - 7.5 * \rho_{480} + 1}$ | Huete et al. (1997) |
| MTCI | MERIS Terrestrial Chlorophyll Index | $\frac{\rho_{754} - \rho_{709}}{\rho_{709} + \rho_{681}}$ | Dash and Curran (2004) |
| Vog | Vogelmann Index | $\frac{\rho_{740}}{\rho_{720}}$ | Vogelmann, Rock, and Moss (1993) |
| SAVI | Soil Adjusted Vegetation Index | $\frac{\rho_{800} - \rho_{670}}{\rho_{800} + \rho_{670} + 0.5} * 1.5$ | Huete et al. (1992) |
| MSAVI | Modified Soil Adjusted Vegetation Index | $\frac{2\rho_{860} + 1 - \sqrt{(2\rho_{860} + 1)^2 - 8(\rho_{860} - \rho_{650})}}{2}$ | Qi et al. (1994) |
| TSAVI | Transformed Soil Adjusted Vegetation Index | $\frac{a(\rho_{860} - \rho_{680}) - b}{a * \rho_{860} + \rho_{680} - ab + X(1 + a^2)}$ $a = 1.22, b = 0.03, X = 0.08$ | Baret and Guyot (1991) |

the optimal values of hyperparameters for a given machine learning model (Bergstra and Bengio, 2012). We searched over a wide range of commonly used hyperparameters for PLSR, RFR and SVR based on extensive literature review. During the grid search, we also enabled a 5-fold cross-validation to ensure that the performance of the model is evaluated effectively across different subsets of the data. Since a wide range of features were used to model the statistical machine learning models (i.e., 269 features for ML-Raw and 22 features for ML-VI), an automatic feature selection mechanism was also introduced in the pipeline. During the training of SVR, 10 best features were selected using the 'Select K-best' function of Scikit-learn using the Pearson's Correlation Coefficient. This selection was done with only the training set, which ensured the robustness of the test set in evaluating the models' performance. However, no feature selection was performed for the PLSR and RFR. Since PLSR performs Principal Component Analysis (PCA) before conducting the regression analysis, the feature space gets reduced to important principal components and reduces the chances of overfitting from higher number of feature space. Also, the number of components is a hyperparameter for the PLSR that was tuned using the grid-search method to maintain the model robustness. On the other hand, RFR calculates the feature importance scores for each feature and avoids multicollinearity specifically for handling hyperspectral remote sensing data (Bhadra et al., 2020), i.e., gives less importance to similar features in the modeling scheme. Therefore, we did not perform any feature selection for RFR either. The statistical machine learning models were trained in a Windows computer with Intel Xeon Platinum E5 (3.1 GHz) that has 8 cores, and 128 GB of RAM. We utilized the parallel processing functionalities of Scikit-learn functions that reduced the amount of training time significantly.

#### 3.6.2. Training DSNNs

We considered a variety of DSNN in our study, i.e., PROSAIL-Net base model, PROSAIL-Net transfer learning models, with many different combinations of architectures (i.e., MLP, LSTM, GRU, and CNN) to process the spectral data. The DSNN training and evaluation was performed using the TensorFlow API (v2.6.0) in Python. First, we created a unique data generator object to automatically process the input pipeline of solar-sensor geometry and spectral data. The data generator allowed us to efficiently read the massive amount of PROSAIL simulation data in batches and ensured efficient use of memory during the training. Since our task is a regression problem, we used the mean squared error as the loss function for all models. The deep learning model also has some hyperparameters to tune, such as, batch size, learning rate, and number of epochs. We used a batch size of 32 for all the model training. The popular 'Adam' optimizer was used for the backpropagation which requires learning rate as its one of the parameters. To avoid searching over different learning rate values, we started with a learning rate of 0.001 and exponentially reduced the value if the epoch exceeds certain iterations. The number of epochs was set as 400 for all DSNNs but it was controlled with an early stopping criterion. We divided the training set for the DSNN into another two sets, i.e., training (70 %) and validation (30 %), where the validation set helps us to understand the bias-variance tradeoff of the models. The early stopping enables the models to automatically stop training if the loss of validation set does not decrease after 15 iterations. The use of a fixed batch size, automatic reduction of learning rate and early stopping criterion helped us to avoid expensive grid search of the hyperparameter tuning. The DSNNs were trained in a Windows computer with Intel Xeon Platinum 8168 (2.7 GHz) 24 processors, 512 GB of RAM, and a Nvidia RTX 8000 graphical processing unit (GPU) with 48 GB memory.

#### 3.6.3. Model evaluation

The performance of both statistical machine learning and DSNNs were evaluated using three commonly used regression metrics, i.e., $R^2$, root mean squared error (RMSE) and normalized root mean squared error (NRMSE), of the corresponding test set. The equations are as given below:

$$R^2 = 1 - \frac{\sum_{i=1}^{n}(y_i - \hat{y}_i)^2}{(y_i - \bar{y}_i)^2} \tag{16}$$

$$RMSE = \sqrt{\frac{\sum_{i=1}^{n}(y_i - \hat{y}_i)^2}{n-1}} \tag{17}$$

$$NRMSE = \frac{RMSE}{\bar{y}} * 100 \tag{18}$$

where, $i = 1, 2, \cdots\cdots, n$ is the test sample, $\hat{y}_i$ and $y_i$ are predicted and measured target variables, respectively, and $\bar{y}$ is the average of each measurable variable. However, in terms of multi-angular DSNN (i.e., PROSAIL-Net-MA), the prediction from multiple angular samples were averaged together to get one prediction value for each sample plot.

## 4. Results

### 4.1. Descriptive statistics of target variables

The target variables considered in this study was the LCC (in $\mu g/cm^2$) and the ALA (in Degrees). Table 4 shows the descriptive statistics of each variable for the entire study area, whereas Fig. 6a illustrates the distributions. The number of samples for ALA ($n = 601$) was higher than LCC ($n = 200$), among which 199 sample plots had both observation of LCC and ALA. The distribution of LCC shows a normal distribution (Fig. 6a), which also appeared as statistically significant (with 99 % confidence interval) in the normality test of D'Agostino and Pearson (1973). Alternatively, ALA shows a slight positive skewness in its spread. The overall spread of ALA distribution is found higher than LCC (Fig. 6a), which is also evident in its relatively higher standard deviation, range, and interquartile range values (Table 4). Lastly, Fig. 6b shows whether there exists any intercorrelation between the two target variables. Based on the Pearson's correlation coefficient and Fig. 6b, it seems there is no correlation between LCC and ALA.

### 4.2. Sensitivity analysis of reflectance

The sensitivity analysis between the reflectance spectra from PROSAIL and UAV with the target variables can reveal the justification for using PROSAIL spectra along with UAV spectra for crop biophysical parameter estimation. We calculated the Pearson's correlation coefficient between the target variables and the direct reflectance from the ach wavelength in both PROSAIL and UAV spectra (Fig. 7a-b). Additionally, the Normalized Difference Spectral Index between a pair of wavelengths from both PROSAIL and UAV was also correlated with the target variables (Fig. 7c-d).

The pattern of correlation between individual wavelength reflectance and LCC (Fig. 7a) for both PROSAIL and UAV seems to follow the similar pattern. However, the magnitude of correlation coefficient for UAV spectra is much lower than the PROSAIL spectra. The wavelength region between 550 nm and 800 nm seems highly informative in

**Table 4**
Descriptive statistics of LCC and ALA.

| Statistics | LCC ($\mu g/cm^2$) | ALA (Degrees) |
|---|---|---|
| Number of Samples | 200 | 601 |
| Minimum | 19.03 | 1.67 |
| Mean | 41.55 | 32.89 |
| Median | 41.61 | 30.83 |
| Maximum | 58.08 | 80.00 |
| Standard Deviation | 7.07 | 12.96 |
| Range | 39.05 | 78.33 |
| Interquartile Range | 8.06 | 16.67 |

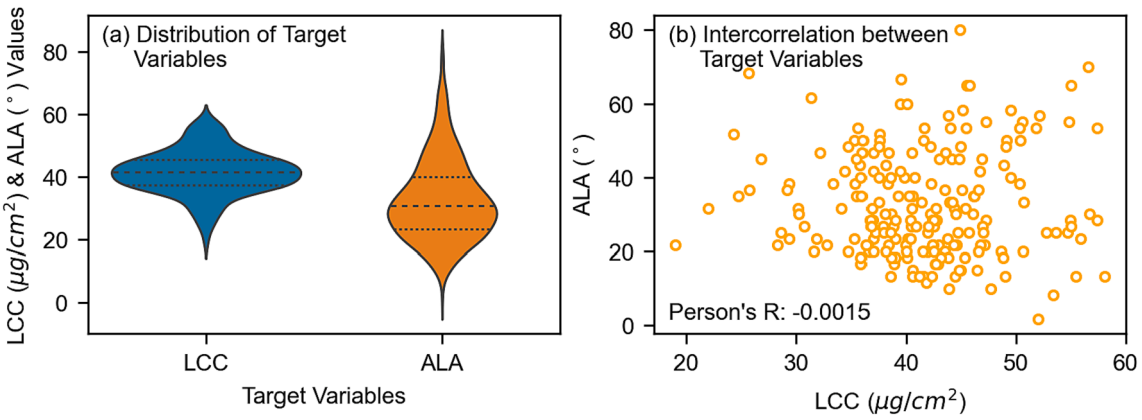


**Fig. 6.** Descriptive statistics of the target variables. (a) Shows the violin plot of LCC and ALA, where the dashed line (– – –) indicates the median and dotted line (···) represents the 25th and 75th percentile of the data. (b) shows the scatterplot between the two target variables, which does not show any correlation between them.

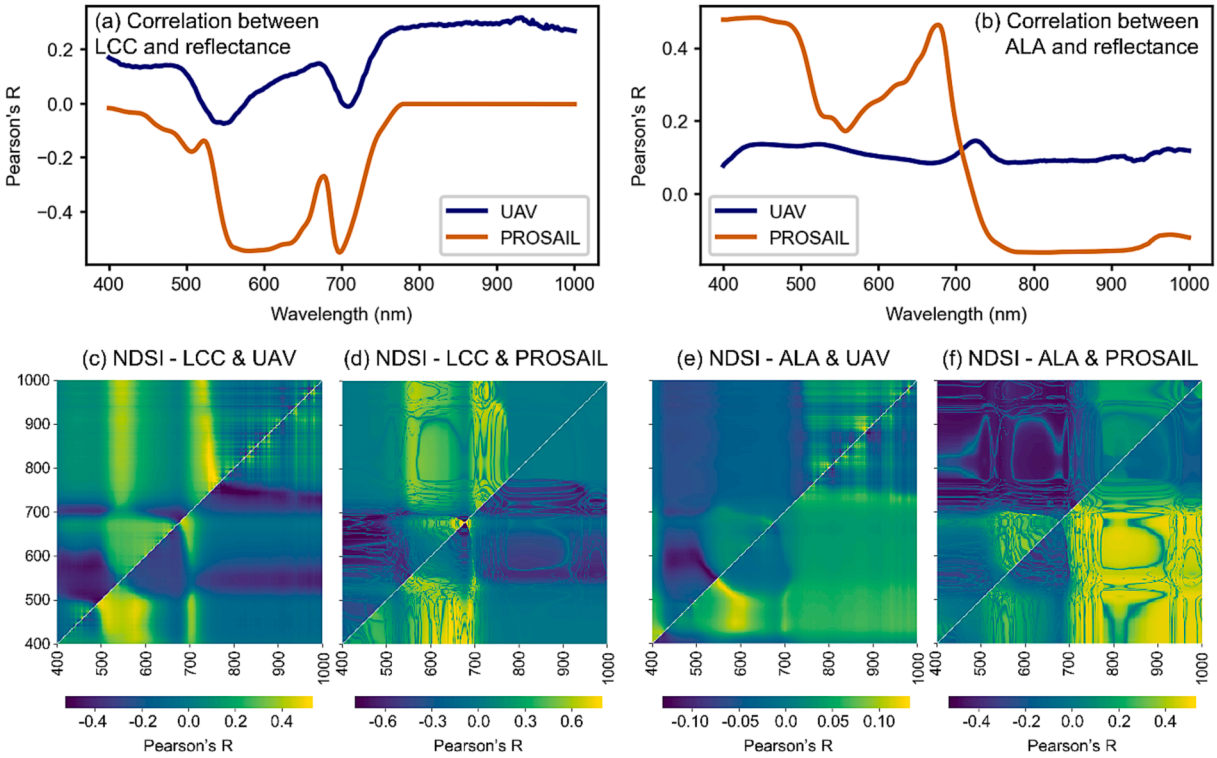


**Fig. 7.** Sensitivity analysis between the spectra and target variables, i.e., Pearson's correlation coefficient between LCC (a), ALA (b) and reflectance spectra from both PROSAIL and UAV; correlation between Normalized Difference Spectral Index (NDSI) of UAV reflectance and LCC (a), PROSAIL reflectance and LCC (b), UAV reflectance and ALA (c) and PROSAIL reflectance and ALA (f).

explaining the variation of LCC. Specifically, the red (~660 nm) and red-edge (~710 nm) shows peak negative correlation (Pearson's R≈-0.5) for PROSAIL spectra. Similar pattern is also observable in terms of the correlation between Normalized Spectral Difference Index (NDSI) and LCC (Fig. 7c-d). NDSI is the ratio of $\rho_a - \rho_b$ and $\rho_a + \rho_b$, where $\rho_a$ and $\rho_b$ are the reflectance of two corresponding wavelengths of $a$ and $b$, that enhances the relationship between a target variable and a pair of wavelengths. Fig. 7c suggests that the NDSI values significantly improved the correlation between UAV and LCC compared to the values achieved by single wavelengths (Fig. 7a). Also, the pattern between UAV NDSI (Fig. 7c) and PROSAIL NDSI (Fig. 7d) looks similar with the only difference between increased Pearson's R values for PROSAIL. Overall, the wavelength pairs of green (~500 nm) and blue (~450 nm) shows positive, whereas red-edge (~700 nm) and red (~650 nm) pairs show negative correlation with LCC. Additionally, some negative correlation can be also seen in the pairs of red-edge and NIR (~800 nm) along with green and NIR.

On the other hand, the relationship between reflectance and ALA (Fig. 7b) seems insignificant (0.0 < Pearson's R < 0.2) for UAV, whereas PROSAIL shows peak positive correlation at the blue (450 – 500 nm) and red region (695 – 700 nm). For the correlation between NDSI and ALA (Fig. 7e-f), the green and red pair as well as the NIR and red pair show a strong correlation with ALA for both UAV and PROSAIL.

### 4.3. PROSAIL-Net performance on simulation data

The proposed PROSAIL-Net consists of two types of training, i.e., the PROSAIL-Net base model, which is trained on PROSAIL-simulated data, and the PROSAIL-Net transfer learning model, which is trained on limited UAV data using the pretrained PROSAIL-Net base model. The

PROSAIL-Net has two branches in its architecture, where one branch handles the solar-sensor angle data, and the other branch processes the spectra data. We experimented the performance of different neural networks in the spectral branch along with the solar-sensor angle branch to estimate LCC and ALA of simulation data. Table 5 shows the performance of PROSAIL-Net base model with different spectral branch on PROSAIL-simulated test set ($n = 30,000$).

Table 5 suggests that the best performance was achieved by the CNN architecture for predicting both LCC ($R^2$ 0.98, NRMSE 1.34 %) and ALA ($R^2$ 0.86, NRMSE 17.44 %). The performance for both target variables were followed by GRU, LSTM, and MLP. Overall, the PROSAIL-Net base model showed better performance for LCC estimation rather than ALA prediction in all type of DSNN spectra branch. Since the CNN architecture consistently outperformed the other networks, we chose CNN as the basis of DSNN spectra branch for the rest of the analysis.

### 4.4. Performance of models on actual data

The performance of different modeling techniques for the LCC and ALA prediction from actual UAV-born data is provided in Table 6. Fig. 8 shows the test $R^2$ of different modeling approaches in different bars. The modeling strategies can be broadly divided into 5 segments, such as, ML-Raw is the statistical machine learning algorithms (i.e., PLSR, RFR, and SVR) with raw reflectance data from all wavelengths; ML-VI is also the statistical machine learning algorithms with 24 vegetation indices (VIs) specified in Table 3; DSNN-Raw is the neural network model directly trained on the UAV-spectra data and angle parameters, PROSAIL-Net-NAD is the DSNN model pretrained by PROSAIL simulation model but using only the NADIR view observations from UAV; and finally the PROSAIL-Net-MA that is same as PROSAIL-Net-NAD but considering multi-angular observations during the training.

The modeling results suggest that the prediction performance of LCC was higher than that of ALA. Without using pretrained PROSAIL-Net, none of the models could predict ALA (Fig. 8b). Among the statistical machine learning algorithms, ML-VI models outperformed the performance ML-Raw models. All three models (i.e., PLSR, RFR, and SVR) showed improved results when using VIs as model input instead of direct wavelength reflectance. However, PLSR tends to perform better ($R^2$ 0.37) than the other models (RFR $R^2$ 0.19 and SVR $R^2$ 0.12) when no feature engineering was performed. However, both RFR and SVR slightly outperformed PLSR when fewer independent features engineered by VIs were used as model input.

The DSNN-Raw was trained using UAV-based reflectance and angle information as input and actual ground truth information collected from field measurements as output. Different types of neural networks for the spectral branch were also considered. While MLP, LSTM and GRU all suffered from poorer performance in predicting LCC from observed data, CNN outperformed the others ($R^2$ 0.44). However, the DSNN-Raw models could not learn any significant pattern to estimate ALA from the observable data (Fig. 8b).

**Table 5**
Performance of PROSAIL-Net base model on PROSAIL-simulated test set.

| Biophysical Parameter | Data set | Metrics | DSNN Spectra Branch MLP | LSTM | GRU | CNN |
|---|---|---|---|---|---|---|
| LCC | Test | $R^2$ | 0.93 | 0.95 | 0.95 | **0.98** |
| | | RMSE | 4.55 | 3.96 | 3.99 | **1.34** |
| | | NRMSE | 11.40 | 9.92 | 9.99 | **3.35** |
| | Train | $R^2$ | 0.96 | 1.00 | 1.00 | 1.00 |
| | | RMSE | 2.96 | 0.61 | 0.55 | 0.28 |
| | | NRMSE | 7.41 | 1.53 | 1.36 | 0.69 |
| ALA | Test | $R^2$ | 0.69 | 0.76 | 0.79 | **0.86** |
| | | RMSE | 12.90 | 11.32 | 10.65 | **8.71** |
| | | NRMSE | 25.81 | 22.66 | 21.30 | **17.44** |
| | Train | $R^2$ | 0.78 | 0.83 | 0.88 | 0.93 |
| | | RMSE | 10.77 | 9.54 | 8.31 | 7.09 |
| | | NRMSE | 21.56 | 19.10 | 16.65 | 14.19 |

The model performance from UAV observed data was significantly improved by using pretrained PROSAIL-Net models for both LCC and ALA prediction. When only the single nadir view data was used in the PROSAIL-Net models (i.e., PROSAIL-Net-NAD), the MLP, LSTM and GRU network showed a large improvement from the DSNN-Raw models. However, the CNN-based PROSAIL-Net-NAD model significantly improved the result of ALA ($R^2$ 0.35) and LCC ($R^2$ 0.52) prediction. This indicates that the use of transfer learning helped the models perform better by utilizing PROSAIL-simulation knowledge. However, the utilization of multi-angular observation during the transfer learning (PROSAIL-Net-MA) improved the prediction performance even more for all types of neural network architecture. For LCC, the highest performance was achieved by the PROSAIL-Net-MA with CNN ($R^2$ 0.66), and a similar result was also observed for the ALA prediction ($R^2$ 0.57). Although the PROSAIL-Net-MA models with MLP, LSTM, and GRU did not improve the performance for ALA prediction compared to the PROSAIL-Net-NAD modes. Therefore, we have identified that the transfer learning enabled PROSAIL-Net model with multi-angular observation and CNN as the spectral architecture can accurately predict LCC and ALA compared to other data-driven approaches. Fig. 9 explains the prediction performance of PROSAIL-Net-MA for LCC and ALA focusing on the error distribution.

The prediction performance of PROSAIL-Net-MA on the LCC test set clearly indicates some underprediction pattern for the relatively higher values (Fig. 9a). For the lower values, the model could predict with better accuracy. Similarly, the model overpredicts the lower ALA values, whereas it underpredicts the extreme values (Fig. 9b). The standardized residual plot can also indicate potential issues related to a regression model. The residual of LCC (Fig. 9c) and ALA (Fig. 9d) appear to be quite randomly distributed near the baseline ($y = 0$) which indicates that the PROSAIL-Net-MA was complex enough to capture the non-linearity within the data.

## 5. Discussion

### 5.1. Comparison between PROSAIL and UAV spectra

We analyzed the direct relationship between PROSAIL-simulated and UAV-extracted spectra with the two target variables, i.e., LCC and ALA. The analysis suggests the similarities of both PROSAIL and UAV spectra in terms of their linear relationship with the target variables. However, the linearity between different independent features and crop traits is often not sufficient enough to develop predictive models as there could exist non-linear relationships (Furbank et al., 2021, Ma et al., 2001, Garriga et al., 2017). However, the sensitivity analysis provides a justification for using PROSAIL-pretrained deep learning model to UAV-extracted hyperspectral spectra.

The magnitude of correlation between UAV-generated spectra and LCC was significantly lower than the correlation between PROSAIL-simulated spectra and LCC (Fig. 7a). The major reason behind this difference could result from the lower sample size for observed data ($n = 200$) compared to PROSAIL simulation ($n = 100,000$). However, the pattern of the relationship for UAV (i.e., the positive and negative peaks) seems to match with PROSAIL for explaining LCC. The sensitive wavelengths identified by this analysis (i.e., 550 – 650 nm, 680 – 710 nm) also agrees with findings from other literature. For instance, Klimov, Klevanik, and Shuvalov (1977) identified the reflectance at 545 nm and 685 nm to be related to pheophytin in the reaction centers of photosystem II, which is an excellent indicator of plant chlorophyll (Lu, 2016). In addition, several studies have identified the red-edge region as the photosystem I absorption spectrum, which is another mechanism involving different chlorophyll-protein complexes (Chen, Quinnell, and Larkum, 2002, Lamb et al., 2002, Kobayashi et al., 1996). In terms of NDSI-based analysis, we found the pair of red-edge and red as highly informative for explaining LCC, which was also identified by Mishra and Mishra (2012) as the basis of Normalized Difference Chlorophyll Index

**Table 6**
Performance of models on the test set for predicting LCC and ALA.

| | | LCC | | | | | | ALA | | | | | |
|---|---|---|---|---|---|---|---|---|---|---|---|---|---|
| | | Test Set | | | Train Set | | | Test Set | | | Train Set | | |
| | | $R^2$ | RMSE | NRMSE | $R^2$ | RMSE | NRMSE | $R^2$ | RMSE | NRMSE | $R^2$ | RMSE | NRMSE |
| ML-Raw | PLSR | 0.37 | 5.06 | 11.78 | 0.46 | 4.81 | 11.10 | 0.04 | 12.09 | 36.06 | 0.46 | 9.03 | 27.23 |
| | RFR | 0.19 | 5.75 | 13.39 | 0.76 | 3.37 | 7.91 | 0.00 | 13.62 | 40.61 | 0.52 | 8.53 | 25.72 |
| | SVR | 0.12 | 5.98 | 13.93 | 0.21 | 6.01 | 13.75 | 0.02 | 12.36 | 36.88 | 0.15 | 11.64 | 35.03 |
| ML-VI | PLSR | 0.43 | 4.79 | 11.16 | 0.54 | 4.43 | 10.25 | 0.00 | 12.35 | 36.83 | 0.43 | 9.29 | 27.98 |
| | RFR | 0.48 | 4.59 | 10.70 | 0.91 | 2.65 | 6.32 | 0.01 | 13.57 | 40.47 | 0.56 | 8.19 | 24.71 |
| | SVR | 0.47 | 4.64 | 10.81 | 0.52 | 4.52 | 10.46 | 0.01 | 12.39 | 36.96 | 0.13 | 11.81 | 35.54 |
| DSNN-Raw | MLP | 0.05 | 7.02 | 16.37 | 0.19 | 6.10 | 13.96 | 0.03 | 13.04 | 39.91 | 0.43 | 9.29 | 27.98 |
| | LSTM | 0.03 | 6.58 | 15.34 | 0.12 | 6.44 | 14.71 | 0.03 | 12.92 | 39.54 | 0.32 | 10.21 | 30.75 |
| | GRU | 0.04 | 6.82 | 15.90 | 0.14 | 6.34 | 14.50 | 0.03 | 12.90 | 39.48 | 0.27 | 10.63 | 32.01 |
| | CNN | 0.44 | 4.87 | 11.36 | 0.54 | 4.43 | 10.25 | 0.03 | 12.84 | 39.30 | 0.21 | 11.13 | 33.52 |
| PROSAIL-Net-NAD (Nadir view) | MLP | 0.41 | 5.19 | 12.12 | 0.51 | 4.57 | 10.57 | 0.07 | 12.07 | 36.22 | 0.15 | 11.64 | 35.03 |
| | LSTM | 0.47 | 4.72 | 11.02 | 0.59 | 4.19 | 9.72 | 0.19 | 11.27 | 33.81 | 0.46 | 9.03 | 27.23 |
| | GRU | 0.36 | 5.33 | 12.46 | 0.48 | 4.71 | 10.88 | 0.12 | 11.75 | 35.25 | 0.43 | 9.29 | 27.98 |
| | **CNN** | **0.52** | **4.63** | **10.81** | **0.68** | **3.76** | **8.76** | **0.35** | **10.10** | **30.30** | **0.65** | **7.44** | **22.45** |
| PROSAIL-Net-MA (Multiangular view) | MLP | 0.52 | 4.75 | 11.08 | 0.69 | 3.71 | 8.65 | 0.06 | 12.08 | 36.02 | 0.24 | 10.88 | 32.77 |
| | LSTM | 0.59 | 4.07 | 9.47 | 0.76 | 3.37 | 7.91 | 0.25 | 10.83 | 32.30 | 0.53 | 8.45 | 25.47 |
| | GRU | 0.50 | 4.53 | 10.55 | 0.65 | 3.90 | 9.08 | 0.12 | 11.62 | 34.67 | 0.44 | 9.20 | 27.73 |
| | **CNN** | **0.66** | **3.78** | **8.81** | **0.81** | **3.13** | **7.38** | **0.57** | **8.15** | **24.32** | **0.71** | **6.93** | **20.94** |

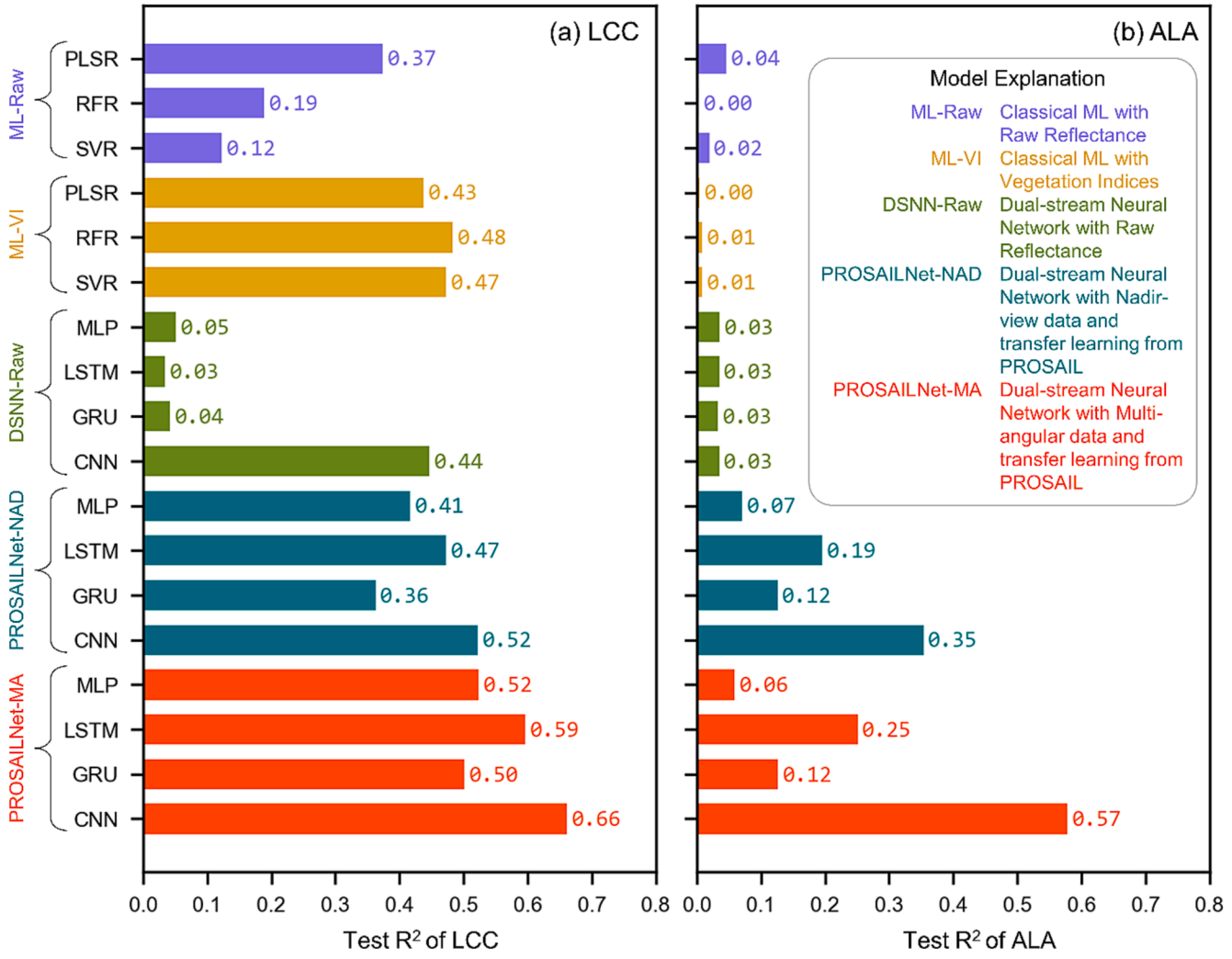


**Fig. 8.** Model performance on actual data for predicting (a) LCC and (b) ALA. The explanations of different model categories are given in (b). The CNN architecture in the PROSAIL-Net along with multi-angular (MA) data outperforms all other models.

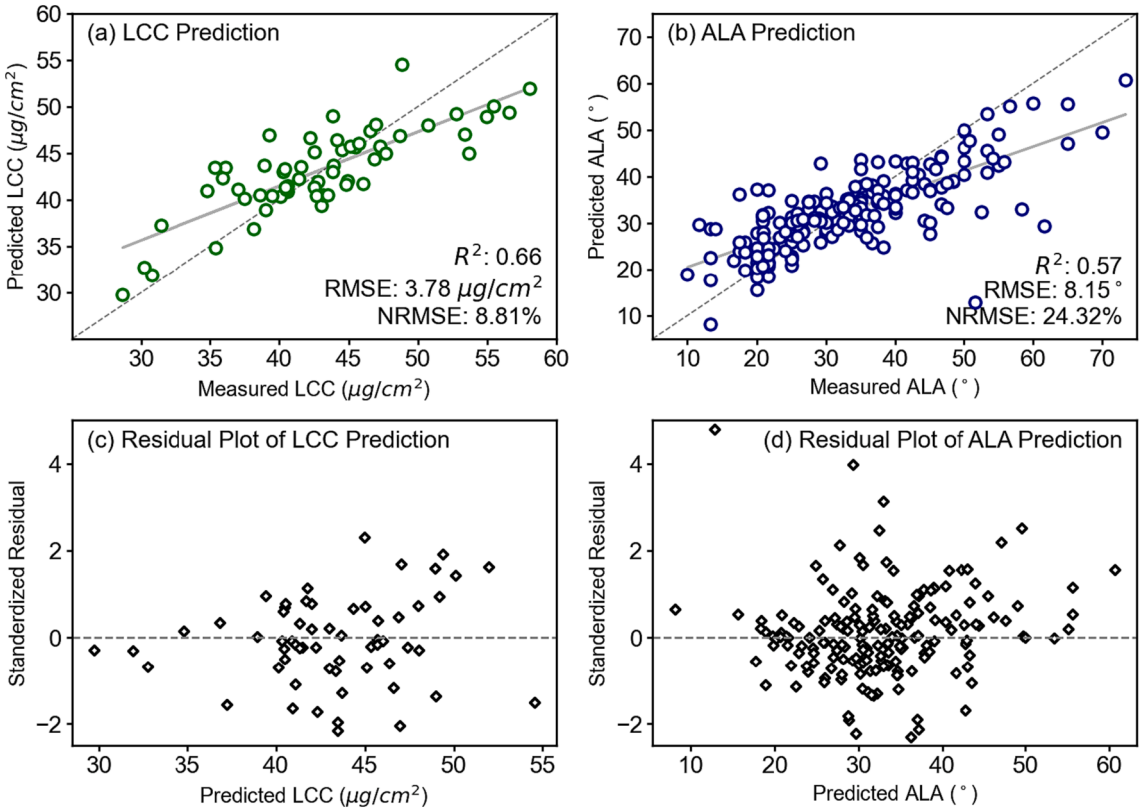


**Fig. 9.** Prediction performance of PROSAIL-Net-MA for LCC and ALA, where the scatterplots between measured and predicted values for LCC (a) and ALA (b); and corresponding standardized residual plot of LCC (c) and ALA (d).

(NDCI) developed for MERIS satellite. Use of normalized indices paired with different bands and red-edge was also highlighted by several studies to explain the LCC variance in plants (Ju et al., 2010, Li et al., 2014, Thompson et al., 2019).

The relationship between reflectance and ALA of crop canopies is not well-explored in the literature. However, Huang et al. (2006) identified the canopy reflectance at 680 nm as an influencing factor for lead angle distribution, which was also found and significant in our study for ALA explanation (Fig. 7b). Alternatively, leaf area index (LAI) has been found as to be highly correlated with ALA (Chen and Black, 1992,1991), which has been widely explored by remote sensing features in the scientific community. For example, the ratio and difference indices derived from green, red, and NIR has been identified as important features for LAI estimation in many different studies (Bouman, 1992, Yu et al., 2020, Siegmann and Jarmer, 2015, Vina et al., 2011).

### 5.2. *Effectiveness of deep transfer learning*

One of the key advantages of deep learning algorithms over statistical machine learning methods, particularly in the realm of high-dimensional hyperspectral data, is the ability to perform automatic feature extraction. Numerous studies have highlighted the use of different dimensionality reduction techniques before the predictive modeling, such as, principal component analysis or PCA (Farrell and Mersereau, 2005, Jiang et al., 2018), singular value decomposition or SVD (Menon, Du, and Fowler, 2016, Ma et al., 2019), and linear discriminant analysis or LDA (Jayaprakash et al., 2020, Fabiyi et al., 2021). PLSR is a multivariate regression technique that automatically performs PCA before generating a predictive model (Godoy, Vega, and Marchetti, 2014), which was found to be very effective in our results. We can see that PLSR perform relatively well ($R^2$ 0.37) compared to RFR ($R^2$ 0.19) or SVR ($R^2$ 0.12) when high-dimensional hyperspectral wavelengths are considered as the input feature space (i.e., ML-Raw in Fig. 8). Many studies have also identified the effectiveness of PLSR for regression tasks based on hyperspectral data (Meacham-Hensold et al., 2019, Gomez, Lagacherie, and Coulouma, 2008, Shen et al., 2020, Zhou et al., 2018). However, when vegetation indices (VIs) were extracted and used as the independent variables for modeling, RFR ($R^2$ 0.48) and SVR ($R^2$ 0.47) tend to perform slightly better than PLSR ($R^2$ 0.43). Therefore, the importance of using different VIs opposed to direct reflectance has been well explored in many literatures when data-driven machine learning algorithms are the point of concern (Selvaraj et al., 2020, Khan et al., 2018, Koh et al., 2022, Richardson,Duigan,and Berlyn, 2002). However, attention should be given to the type of target variables in the analysis and VIs relating to that target variable should be used.

On the other hand, deep neural networks offer the capability of automatic feature extraction through their network of neurons. Several studies have explored such feature extraction capabilities, specifically for hyperspectral data in terms of image classification and regression (Zhao and Du, 2016, Chen et al., 2016, Chen et al., 2014, He et al., 2017). However, the issue of having large training dataset in deep neural networks remains a challenge (Nguyen et al., 2021, Liu and Xiao, 2020), specifically for agricultural decision making. Therefore, we have demonstrated the potential of large training samples extracted by PROSAIL-simulation and transfer learning in the context of plant trait extraction and achieved significant performance improvement. Our DSNN, which is the basis of PROSAIL-Net was first trained with the limited observed sample for estimating LCC ($n$ = 140) and ALA ($n$ = 492). The DSNN only performed relatively well for predicting LCC, when the 1D CNN architecture was considered as the spectral branch ($R^2$ 0.52). However, there was no knowledge gain for explaining the ALA by any of the architectures considered in DSNN-Raw. One the other hand, the test accuracy for the DSNN models (i.e., PROSAIL-Net base model in Table 3) showed significant improvement, specifically for predicting LCC ($R^2$ 0.98 and NRMSE 3.35 %). Although the result for ALA was not as good as LCC, the CNN-based DSNN still could explain 86 % variance

of the unseen ALA samples. Later we used the pretrained DSNN for the limited observed data and achieved performance improvement for both LCC and ALA, specifically when CNN was considered as the spectral branch architecture.

The use of 1D CNN as an excellent feature extractor for hyperspectral image processing has been reported by many literatures (Zhang et al., 2017, Gao et al., 2021, Du et al., 2022, Li, Cui, et al. 2019, Huang, He, et al. 2022). The convolution operation in CNN prioritizes in capturing local patterns in the input data (Lopez Pinaya et al., 2020), whereas the MLP, LSTM or GRU struggle to understand the long-term dependencies. For 2D images, the objective of convolution operation is to identify textural or structural patterns within the image and discard unnecessary information by reducing the feature map while the network progresses (Lo et al., 1995). Similarly, 1D convolution tries to highlight uncorrelated spectral features from the high-dimensional spectral data and find optimum kernel weights through back-propagation (Kiranyaz et al., 2021). For example, the variation of reflectance values at 450 nm and 455 nm might not be critical enough for explaining a certain target variable, which could suggest the use of only one feature instead of both during the model training. The 1D kernel in the CNN can learn this unique feature through a large training database and only captures relevant information from fewer features. In our result, we have also seen the superiority of 1D CNN over MLP, LSTM or GRU networks. The CNN-based PROSAIL-Net network was later leveraged to transfer the learned knowledge from a simulated dataset into an observable space through UAV-based hyperspectral imaging.

The objective of transfer learning is to let a machine learning model leverage the knowledge learned from source tasks in different domains, so the model already knows about the relationship between independent and dependent variables (Pan et al., 2011, Pan and Yang, 2010). Numerous studies have leveraged deep transfer learning to solve problems in image classification (Shaha and Pawar, 2018, Quattoni, Collins, and Darrell, 2008), object detection (Talukdar et al., 2018, Bu et al., 2021), natural language processing (Raffel et al., 2020, Houlsby et al., 2019), sentiment analysis (Huang, Zhang, et al. 2022, Tao and Fang, 2020), etc. In our study, the transfer learning mechanism is homogeneous and straightforward. Since the feature space of PROSAIL-simulated and UAV-extracted were same, we could simply use the entire pre-trained model from PROSAIL in the UAV-observed data space. For LCC, our result shows that the PROSAIL-Net with multi-angular data improved the model performance significantly compared to training from scratch (i.e., DSNN-Raw) or statistical machine learning algorithms (i.e., ML-Raw and ML-VI). However, the performance of ALA was way more consequential when pretrained PROSAIL-Net was used. Our results show that none of the statistical machine learning algorithms or DSNN-Raw models could learn to predict ALA from spectral data. Due to the massive amount of training data generated by PROSAIL-simulation, our proposed DSNN with CNN learned the appropriate relationship between spectral data, solar-sensor geometry angle data and ALA. We have not found many studies that used PROSAIL-inversion to estimate the ALA other than Lunagaria and Patel (2019) and Tripathi et al. (2012). However, both studies relied on inefficient lookup table based inversion method using either satellite (Tripathi et al., 2012) or goniometer (Lunagaria and Patel, 2019), which are not practical in terms of plot-level decision making. On the other hand, our study provides a cost-effective high-throughput solution to estimate two major crop biophysical parameters by transforming cross-grid UAV data into goniometer like multi-angular data.

In terms of transfer learning and PROSAIL-inversion for crop biophysical trait estimation, we have found only one study (Zhang et al., 2021) in the literature. While (Zhang et al., 2021) highlighted the efficiency of transfer learning strategy with PROSAIL-simulation and ground/UAV-based observations for LCC estimation, we identified some major gaps in the process. For instance, the effect of different architecture in the modeling process was not well explored. In addition, the methodology required the use of ground-based spectroscopic measurement, which is often hard to collect in a large agricultural experiment. Moreover, the study used 'sigmoid' activation function in the final output layer of the MLP model, which is questionable as the output of 'sigmoid' is a probability distribution and suitable for classification tasks. We argue that the activation function in the final output layer for a regression task should be a linear function, such as, ReLU or simply the output of the last dense layer. Numerous studies have also reported the use of ReLU or linear activation function in the final layer when the target is a continuous variable (Maimaitijiang et al., 2020, Nevavuori, Narra, and Lipping, 2019, Chu and Yu, 2020). Our study on the other hand, investigated many different spectral branch architectures and identified that CNN works well in extracting meaningful information from spectral data. We have also used specific features that can be easily collected in a real-world scenario. For example, the solar-sensor angle geometry information can be easily extracted by the end-to-end pipeline developed by Bhadra et al. (2022). Additionally, the only the spectral data was the required input for the PROSAIL-Net, which can also be easily extracted by the UAV hyperspectral cubes.

### 5.3. Influence of multi-angular observations

Our result clearly identifies the effectiveness of having multi-angular observations in the PROSAIL-Net model. When PROSAIL-Net-MA models were used to estimate LCC and ALA, the performance improved significantly from the PROSAIL-Net-NAD models (Fig. 8). Many studies performing PROSAIL-inversion have also identified the importance of having multi-angular hyperspectral observations (Lunagaria and Patel, 2019, Weiss et al., 2000, Atzberger, 2004). The reason lies behind the fundamentals of bi-directional reflectance distribution function (BRDF), which characterizes how light is reflected from an object or surface (Buchhorn, Raynolds, and Walker, 2016, Hou et al., 2019). The relationship between solar reflection and an object depends on the angle of the incoming light relative to the Earth's surface (i.e., solar zenith angle, $\theta_s$) and the angle of the sensor in relation to the surface (i.e., sensor zenith angle, $\theta_v$). In addition to the solar and sensor zenith angles (i.e., $\theta_s$ and $\theta_v$), PROSAIL considers the relative azimuth angle between the sun and sensor ($\phi_{sv}$) as one of its parameters. Therefore, having hyperspectral reflectance information from multiple angles allows the PROSAIL-Net-MA to understand the object properties with more certainty, thus reducing the ill-posed challenge of PROSAIL inversion (Duan et al., 2014, Jay et al., 2017, Roosjen et al., 2018, Sun et al., 2022).

The methodology developed for this study introduces a novel concept of using UAV-borne push-broom hyperspectral camera to capture the varying solar-sensor geometry angles. Roosjen et al. (2017) developed a similar method but used a frame-based hyperspectral camera, which often suffers from several challenges when mounted in a UAV. The post-processing of frame hyperspectral camera is a challenging task as there could be offsets of the bands within individual hyperspectral cube (Honkavaara et al., 2017, Jakob, Zimmermann, and Gloaguen, 2017). Additionally, the larger field of view (FOV) of the frame camera reduces the spectral and spatial resolution of the cube due to the requirement of high energy (Fan et al., 2021). Push-broom hyperspectral cameras on the other hand, provides more accurate data capture with higher spatial and spectral resolution (Aasen et al., 2018). However, the push-broom camera system on a UAV should be equipped with precise GNSS/IMU sensors as the line scanning system of the push broom camera is sensitive to flight dynamics. Also, the use of GNSS/IMU information is used in the post-processing steps to accurately perform the geometric correction and orthorectification. While the inclusion of GNSS/IMU sensors with the push-broom camera increases the overall cost of the system, we used the GNSS/IMU data to extract important sensor geometry angle information. Additionally, the solar angle data relative to the ground pixel coordinates is also precise specifically when highly accurate GNSS information is considered. Fig. 10 shows two sample hyperspectral cubes with different angles. Having access to the

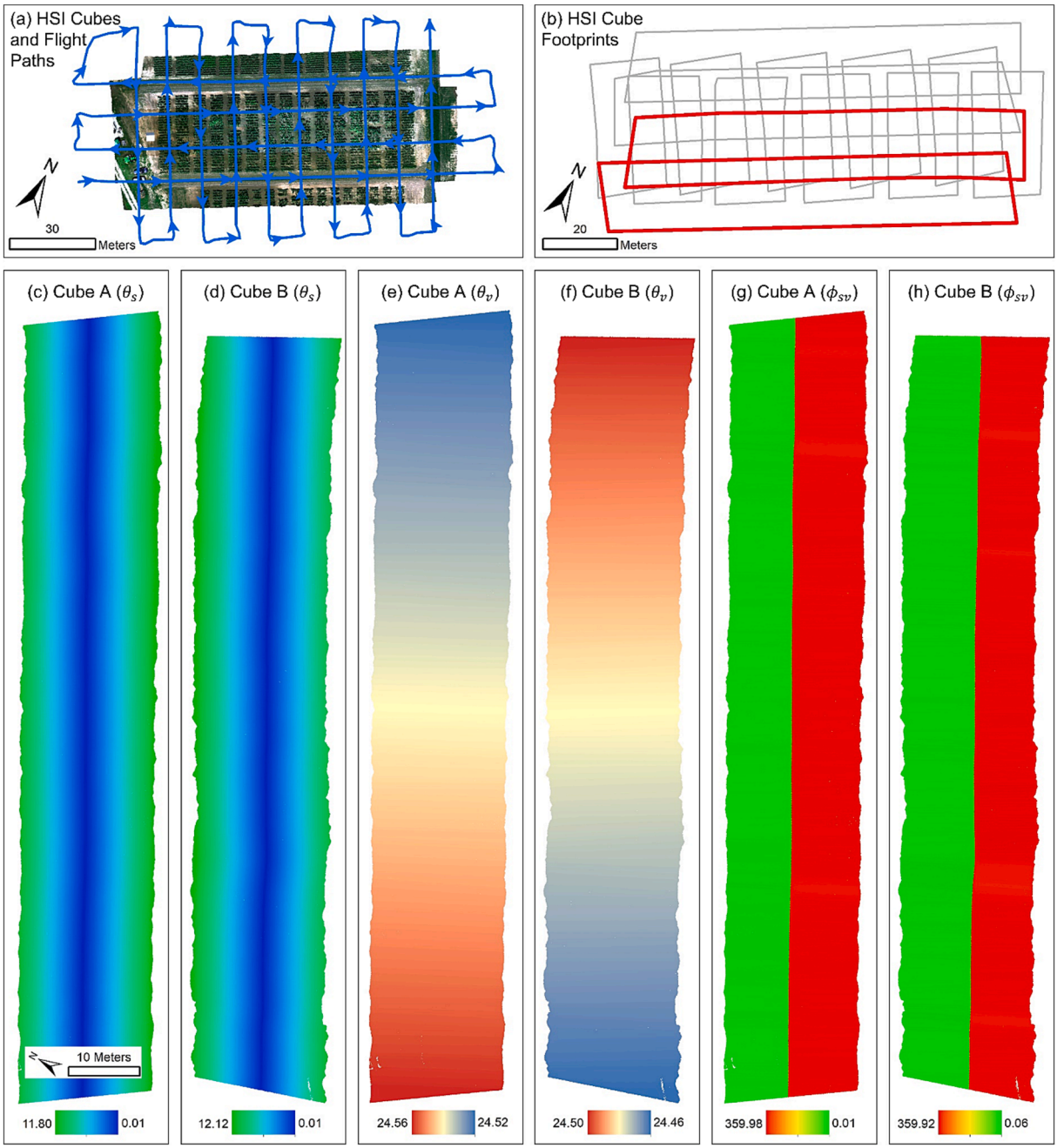


**Fig. 10.** The result of having multi-angular hyperspectral image (HSI) cubes from cross-grid flight pattern. The HSI cubes along with the actual cross-grid flight path is shown in (a), whereas (b) shows the footprints of each cube. The sample image is shown for the D16 field. Two side by side cubes marked (with bold red) in (b) are further expanded to visualize the solar zenith ($\theta_s$), sensor zenith ($\theta_v$), and relative azimuth angle ($\phi_{sv}$) from c-h. (For interpretation of the references to color in this figure legend, the reader is referred to the web version of this article.)

accurate GNSS information allowed us to interpolate angle rasters for each cube.

### 5.4. Limitations

Although we have demonstrated the superior performance of PROSAIL-Net using transfer learning and multi-angular UAV observations for accurate estimation of LCC and ALA, we have identified some limitations within our study.

The major limitation of the proposed methodology is the use of cross-grid flight pattern to acquire multi-angular hyperspectral observation. UAVs equipped with push-broom sensors take more time to capture data since the payload is typically heavier than RGB or multispectral camera systems. Also, such complex UAV system requires flight calibration before and after collecting the actual data, which reduces the data collection time even more. For instance, we used the DJI M600 UAV equipped with a Headwall NanoHyperspec 12 mm VNIR camera system, which can fly up to 20 min with a fully charged battery set. Performing a cross grid flight pattern with that time limit can be challenging specifically when large fields are considered in the experiment. For instance, the D3 (2020) and D16 (2021) fields in Missouri were relatively smaller in size than the U1 field in Illinois (2021). Therefore, we flew the entire cross-grid pattern at D3 and D16 without any issue, but we had to fly two separate flights for the U1 field due to its larger size. Having enough flight time for capturing the multi-angular data from a large experimental field can be challenging when UAV-borne push-broom

hyperspectral system is in consideration. However, capturing data with higher altitude may solve such issues if careful consideration is given to the balance of flight altitude and spatial resolution.

Another challenge of having longer flight time with hyperspectral UAVs is the issue of radiometric calibration. Since hyperspectral sensors are highly sensitive, a pre-flight camera calibration is performed using a factory-standard reflectance panel to determine the exposure and frame rate of the data capture. The exposure and frame rate are determined based on the solar intensity, flight altitude and speed. However, an assumption of solar intensity being the same through the entire flight time is made, which is often challenging when the flight time is longer. Because within a longer timeframe, the possibility of solar intensity being changed increases and that can reduce the quality of the reflectance data. For instance, we had to collect data two times for one experimental day (i.e., July 21, 2021, in D3) because of sudden solar intensity change during the flight. Such issues can hamper the high-throughput nature of data collection in a crop breeding or precision agriculture operation. However, inclusion of a downwelling irradiance sensor on the UAV system and applying novel calibration techniques during the tilting condition can reduce the issue of unprecedented solar condition changes (Koppl et al., 2021).

While the PROSAIL simulation can produce reflectance spectra from 400 to 2500 nm wavelength, we had to only consider the very near-infrared (VNIR) section (i.e., 400 – 1000 nm) during the modeling. Since the hyperspectral sensor considered in our experiment could only capture data in the VNIR region, we had to discard the short-wave infrared (SWIR) region from our analysis. However, reflectance at the SWIR region has been often found as very important in explaining water absorption within the plant leaves, which might be connected to certain biophysical traits (Raya-Sereno et al., 2022, Herrmann et al., 2010, Kandylakis et al., 2020). Therefore, conducting this similar study with a co-aligned VNIR-SWIR hyperspectral camera would have given better performance for predicting LCC and ALA.

Finally, the scope of our study did not allow us to collect sample measurements of other PROSAIL variables, such as, anthocyanin, carotenoid, dry matter content, brown pigments, etc. Availability of such values would have been helpful to perform the sensitivity of knowing such measurement in the PROSAIL-Net training. Moreover, the LCC values were measured using a handheld proximal sensing instrument (i.e., Dualex Scientific) that uses leaf reflectance and transmittance to estimate LCC. Despite the wide usage of proximal sensing techniques to evaluate crop health parameters, such as LCC, calibrating these instruments through laboratory wet analysis remains the preferred approach. Additionally, we could not collect the LCC data for the U1 field on August 17, 2022 due to a technical malfunction of the Dualex instrument. Availability of LCC data would have been better for the model training as the dataset would include ground truths from two different locations for LCC.

### 5.5. Future studies

The potential of merging physical remote sensing models and deep neural networks through transfer learning is enormous in the field of crop breeding and precision agriculture. Future studies should focus on collecting more precise PROSAIL variables and perform PROSAIL-Net operation on other crops in different management conditions. Since we have identified that CNN-based network for spectral data and having multiple viewing angle for UAVs offer more robust learning mechanism, future work can focus on other aspects of the modeling.

In recent times, a new wave of foundational deep learning models have surfaced in many disciplines, aiming to serve as a base model for one task that can be fine-tuned for more specific tasks. For instance, generative pre-trained transformer or GPT (Brown et al., 2020), bidirectional encoder representation from transformer or BERT (Devlin et al., 2019), language model for dialogue applications or LaMDA (Thoppilan et al., 2022), are some of the most popular foundational models for natural language processing that can be fine-tuned for more specific tasks. Similarly, the meteorological community has developed a foundational model named ClimaX that understands the complex relationship between weather variables through physical groundings (Nguyen et al., 2023). The PROSAIL-Net can also become a foundational model after trained with billions of simulated spectra, to enable researchers and scientists worldwide to fine-tune it for more specific vegetation trait retrieval. Furthermore, reinforcement learning can be implemented to allow the pretrained network to continually improve and adapt, based on feedback from the outcomes.

UAV-hyperspectral data, when coupled with the PROSAIL model, helps in understanding various crop biophysical properties. However, adapting UAV-hyperspectral systems for large-scale monitoring presents challenges as it can be expensive and resource-intensive. Satellite-based hyperspectral systems emerge as a potential solution for such monitoring needs. Some hyperspectral satellites, like EnMAP (Guanter et al., 2015) and PRISMA (Loizzo et al., 2018), offer moderate spatial resolution coverage globally, typically around 30 m. Nonetheless, this resolution might not suffice for plot-level crop monitoring. Despite this limitation, upcoming commercial hyperspectral systems promise better ground sampling distance (GSD), thus enabling finer-scale monitoring. On another front, satellite-based multispectral data holds promise for PROSAIL-Net application. However, PROSAIL-Net necessitates high-dimensional spectral data, posing challenges with multispectral reflectance. For instance, missions like Landsat and Sentinel-2 offer around 10–13 bands in the VNIR and SWIR ranges, raising questions regarding their compatibility with PROSAIL-Net without further examination. Moreover, these missions feature relatively coarse spatial resolution (i.e., 10–30 m), potentially unsuitable for precise agricultural applications at the plot level. Commercial satellite missions with increased bands and finer spatial resolution, such as WorldView-3 (Longbotham et al., 2015), with approximately 16 bands and 3-meter spatial resolution, emerge as promising candidates for PROSAIL-Net. Consequently, future research should explore the impact of spectral bands on PROSAIL-Net's performance and determine the optimal balance between the number of bands and accuracy. Such investigations will guide the selection of a suitable multispectral satellite for scalable application of PROSAIL-Net.

The integration of PROSAIL with deep neural networks using transfer learning underscores the potential of combining data-driven approaches with other remote sensing or crop growth models. The use of UAV-based hyperspectral remote sensing in conjunction with other radiative transfer models (RTMs), such as MODTRAN (MODerate resolution atmospheric TRANsmission), which simulates radiation transmission through the atmosphere, reflection, and emission from surfaces, can provide a deeper understanding of crop health (Gail et al., 2000). Likewise, crop growth models, such as DSSAT (Decision Support System for Agrotechnology Transfer), which is capable of simulating the growth of over 40 crops including corn, soybeans, and wheat, can provide crucial information for agricultural management (Jones et al., 2003). The fusion of deep learning, various RTMs, and crop growth models could potentially unleash the power of general intelligence in decision-making for a wide range of agricultural applications.

## 6. Conclusion

In our study we present PROSAIL-Net, a transfer learning-based neural network aimed at accurately and efficiently estimating the LCC and ALA of corn using UAV-borne hyperspectral images. Precision agriculture and crop breeding operations often face challenges due to limited sample sizes when using deep neural networks. Our approach overcomes this challenge by leveraging the vast amount of simulated data from the PROSAIL model. By integrating transfer learning and the PROSAIL model, PROSAIL-Net offers a promising solution for improving the accuracy of crop parameter estimation in precision agriculture and crop breeding applications. Key findings from our study are:

1. 1D CNN architecture exhibits superior performance compared to MLP, LSTM, and GRU networks when utilized in the spectral branch of DSNN. This superiority was demonstrated through the evaluation of both PROSAIL-simulated data and transfer learning scenarios for estimating LCC and ALA.
2. PROSAIL-Net outperforms all other modeling scenarios in predicting LCC ($R^2$ 0.66 and NRMSE 8.81 %) and ALA ($R^2$ 0.57 and NRMSE 24.32 %), which underscores the importance of utilizing large number of PROSAIL-simulated data in conjunction with transfer learning.
3. PROSAIL-Net with multi-angular observations significantly outperformed PROSAIL-Net with only nadir observations for both LCC ($R^2$ improved from 0.52 to 0.66) and ALA ($R^2$ improved from 0.35 to 0.57). This signifies the importance of having multi-angular UAV observations during the application process.

In summary, our study provides a valuable contribution to the field of precision agriculture and crop breeding and highlights the potential of transfer learning and deep learning as a tool for improving crop parameter estimation. Future research can focus on collecting more precise PROSAIL variables and expanding the application of PROSAIL-Net to other crops in varying management conditions. Additionally, the integration of PROSAIL-Net with other remote sensing and crop growth models has the potential to unlock the power of general intelligence in decision-making for a wide range of agricultural applications.

**Funding**

This work was supported by the United States Geological Survey (USGS) AmericaView Grant (G18AP00077); Foundation for Food & Agricultural Research (FFAR # 2331-201-0103); National Science Foundation Plant Genome Research Program (NSF PGRP # 1733606); NSF/USDA NIFA (Grant # 2020-67021-31530); NSF Cyber Physical Systems (CPS award # 2133407); and Sustainable Agriculture and Education (Project #: GNC22-343).

## CRediT authorship contribution statement

**Sourav Bhadra:** Conceptualization, Data curation, Writing - original draft, Visualization, Investigation, Validation, Formal analysis, Project administration, Software. **Vasit Sagan:** Conceptualization, Funding acquision, Writing - review & editing, Investigation, Validation, Methodology, Supervision, Resources, Project administration, Software. **Supria Sarkar:** Writing - review & editing, Visualization, **Maxwell Braud:** Data curation, Writing - review & editing. **Todd C.Mock:** Funding acquision, Writing - review & editing, Supervision, Resources. **Andrea Eveland:** Writing - review & editing, Supervision, Resources.

## Declaration of competing interest

The authors declare that they have no known competing financial interests or personal relationships that could have appeared to influence the work reported in this paper.

## References

Aasen, H., Honkavaara, E., Lucieer, A., Zarco-Tejada, P.J., 2018. Quantitative remote sensing at ultra-high resolution with UAV spectroscopy: a review of sensor technology, measurement procedures, and data correction workflows. Remote Sens. (Basel) 10 (7). https://doi.org/10.3390/rs10071091.

Ajit, A., Acharya, K., Samanta, A., 2020. A review of convolutional neural networks. 2020 International Conference on Emerging Trends in Information Technology and Engineering (ic-ETITE), 24-25 Feb.

Alton, P.B., North, P.R., Los, S.O., 2007. The impact of diffuse sunlight on canopy light-use efficiency, gross photosynthetic product and net ecosystem exchange in three forest biomes. Glob. Chang. Biol. 13 (4), 776–787. https://doi.org/10.1111/j.1365-2486.2007.01316.x.

Annala, L., Honkavaara, E., Tuominen, S., Polonen, I., 2020. Chlorophyll concentration retrieval by training convolutional neural network for stochastic model of leaf optical properties (SLOP) inversion. Remote Sens. (Basel) 12 (2). https://doi.org/10.3390/rs12020283.

Antonucci, G., Impollonia, G., Croci, M., Potenza, E., Marcone, A., Amaducci, S., 2023. Evaluating biostimulants via high-throughput field phenotyping: biophysical traits retrieval through PROSAIL inversion. Smart Agricultural Technology 3, 100067. https://doi.org/10.1016/j.atech.2022.100067.

Arroyo-Mora, J.P., Kalacska, M., Loke, T., Schlapfer, D., Coops, N.C., Lucanus, O., Leblanc, G., 2021. Assessing the impact of illumination on UAV pushbroom hyperspectral imagery collected under various cloud cover conditions. Remote Sens. Environ. 258 https://doi.org/10.1016/j.rse.2021.112396.

Atzberger, C., 2004. Object-based retrieval of biophysical canopy variables using artificial neural nets and radiative transfer models. Remote Sens. Environ. 93 (1–2), 53–67. https://doi.org/10.1016/j.rse.2004.06.016.

Baret, Frédéric, Buis, Samuel, 2008. "Estimating Canopy Characteristics from Remote Sensing Observations: Review of Methods and Associated Problems." In *Advances in Land Remote Sensing: System, Modeling, Inversion and Application*, edited by Shunlin Liang, 173-201. Dordrecht: Springer Netherlands.

Baret, F., Guyot, G., 1991. Potentials and limits of vegetation indices for LAI and APAR assessment. Remote Sens. Environ. 35 (2), 161–173. https://doi.org/10.1016/0034-4257(91)90009-U.

Barnes, E.M., Clarke, T.R., Richards, S.E., Colaizzi, P.D., Haberland, J., Kostrzewski, M., Waller, P., Choi, C., Riley, E., Thompson, T., 2000. Coincident detection of crop water stress, nitrogen status and canopy density using ground-based multispectral data. 5th International Conference on Precision Agriculture and Other Resource Management, Bloomington, MN, USA, July 16-19.

Barnsley, M.J., Settle, J.J., Cutter, M.A., Lobb, D.R., Teston, F., 2004. The PROBA/CHRIS mission: a low-cost smallsat for hyperspectral multiangle observations of the earth surface and atmosphere. IEEE Trans. Geosci. Remote Sens. 42 (7), 1512–1520. https://doi.org/10.1109/Tgrs.2004.827260.

Barreto, M.A.P., Johansen, K., Angel, Y., McCabe, M.F., 2019. Radiometric assessment of a UAV-based push-broom hyperspectral camera. Sensors 19 (21). https://doi.org/10.3390/s19214699.

Bellis, E.S., Hashem, A.A., Causey, J.L., Runkle, B.R.K., Moreno-Garcia, B., Burns, B.W., Green, V.S., Burcham, T.N., Reba, M.L., Huang, X.Z., 2022. Detecting intra-field variation in rice yield with unmanned aerial vehicle imagery and deep learning. Front. Plant Sci. 13 https://doi.org/10.3389/fpls.2022.716506.

Berger, K., Atzberger, C., Danner, M., D'Urso, G., Mauser, W., Vuolo, F., Hank, T., 2018. Evaluation of the PROSAIL model capabilities for future hyperspectral model environments: A review study. Remote Sensing 10 (1). https://doi.org/10.3390/rs10010085.

Bergstra, J., Bengio, Y., 2012. Random search for hyper-parameter optimization. J. Mach. Learn. Res. 13, 281–305. https://doi.org/10.5555/2188385.2188395.

Bhadra, S., Sagan, V., Maimaitijiang, M., Maimaitiyiming, M., Newcomb, M., Shakoor, N., Mockler, T.C., 2020. Quantifying leaf chlorophyll concentration of sorghum from hyperspectral data using derivative calculus and machine learning. Remote Sens. (Basel) 12 (13). https://doi.org/10.3390/rs12132082.

Bhadra, S., Sagan, V., Nguyen, C., Braud, M., Eveland, A.L., Mockler, T.C., 2022. Automatic extraction of solar and sensor imaging geometry from UAV-borne push-broom hyperspectral camera. In: ISPRS Annals of the Photogrammetry, Remote Sensing and Spatial Information Sciences V-3-2022:131–137. https://doi.org/10.5194/isprs-annals-V-3-2022-131-2022.

Bhat, S.A., Huang, N.F., 2021. Big data and AI revolution in precision agriculture: survey and challenges. IEEE Access 9, 110209–110222. https://doi.org/10.1109/Access.2021.3102227.

Blackburn, G.A., 1999. Relationships between spectral reflectance and pigment concentrations in stacks of deciduous broadleaves. Remote Sens. Environ. 70 (2), 224–237. https://doi.org/10.1016/S0034-4257(99)00048-6.

Boggs, J.L., Tsegaye, T.D., Coleman, T.L., Reddy, K.C., Fahsi, A., 2003. Relationship between hyperspectral reflectance, soil nitrate-nitrogen, cotton leaf chlorophyll, and cotton yield: a step toward precision agriculture. J. Sustain. Agric. 22 (3), 5–16. https://doi.org/10.1300/J064v22n03_03.

Borges, M.V.V., Garcia, J.D., Batista, T.S., Silva, A.N.M., Baio, F.H.R., Da Silva, C.A., de Azevedo, G.B., Azevedo, G.T.D.S., Teodoro, L.P.R., Teodoro, P.E., 2022. High-throughput phenotyping of two plant-size traits of eucalyptus species using neural networks. J. For. Res. 33 (2), 591–599. https://doi.org/10.1007/s11676-021-01360-6.

Botha, E.J., Leblon, B., Zebarth, B., Watmough, J., 2007. Non-destructive estimation of potato leaf chlorophyll from canopy hyperspectral reflectance using the inverted PROSAIL model. Int. J. Appl. Earth Obs. Geoinf. 9 (4), 360–374. https://doi.org/10.1016/j.jag.2006.11.003.

Bouman, B.A.M., 1992. Accuracy of estimating the leaf-area index from vegetation indexes derived from crop reflectance characteristics, a simulation study. Int. J. Remote Sens. 13 (16), 3069–3084. https://doi.org/10.1080/01431169208904103.

Breunig, F.M., Galvao, L.S., dos Santos, J.R., Gitelson, A.A., de Moura, Y.M., Teles, T.S., Gaida, W., 2015. Spectral anisotropy of subtropical deciduous forest using MISR and MODIS data acquired under large seasonal variation in solar zenith angle. Int. J. Appl. Earth Obs. Geoinf. 35, 294–304. https://doi.org/10.1016/j.jag.2014.09.017.

Brewer, K., Clulow, A., Sibanda, M., Gokool, S., Naiken, V., Mabhaudhi, T., 2022. Predicting the chlorophyll content of maize over phenotyping as a proxy for crop health in smallholder farming systems. Remote Sens. (Basel) 14 (3). https://doi.org/10.3390/rs14030518.

Brown, T.B., Mann, B., Ryder, N., Subbiah, M., Kaplan, J., Dhariwal, P., Neelakantan, A., Shyam, P., Sastry, G., Askell, A., Agarwal, S., Herbert-Voss, A., Krueger, G., Henighan, T., Child, R., Ramesh, A., Ziegler, D.M., Jeffrey, W.u., Winter, C., Hesse, C., Chen, M., Sigler, E., Litwin, M., Gray, S., Chess, B., Clark, J., Berner, C., McCandlish, S., Radford, A., Sutskever, I., Amodei, D., 2020. Language models are few-shot learners. ArXiv. https://doi.org/10.48550/ARXIV.2005.14165.

Bsaibes, A., Courault, D., Baret, F., Weiss, M., Olioso, A., Jacob, F., Hagolle, O., Marloie, O., Bertrand, N., Desfond, V., Kzemipour, F., 2009. Albedo and LAI estimates from FORMOSAT-2 data for crop monitoring. Remote Sens. Environ. 113 (4), 716–729. https://doi.org/10.1016/j.rse.2008.11.014.

Bu, X., Peng, J., Yan, J., Tan, T., Zhang, Z., 2021. GAIA: a transfer learning system of object detection that fits your needs. 2021 IEEE/CVF Conference on Computer Vision and Pattern Recognition (CVPR).

Buchhorn, M., Raynolds, M.K., Walker, D.A., 2016. Influence of BRDF on NDVI and biomass estimations of Alaska Arctic tundra. Environ. Res. Lett. 11 (12) https://doi.org/10.1088/1748-9326/11/12/125002.

Burkart, A., Aasen, H., Alonso, L., Menz, G., Bareth, G., Rascher, U., 2015. Angular dependency of hyperspectral measurements over wheat characterized by a novel UAV based goniometer. Remote Sens. (Basel) 7 (1), 725–746. https://doi.org/10.3390/rs70100725.

Burud, I., Lange, G., Lillemo, M., Bleken, E., Grimstad, L., From, P.J., 2017. Exploring robots and UAVs as phenotyping tools in plant breeding. IFAC-PapersOnLine 50 (1), 11479–11484. https://doi.org/10.1016/j.ifacol.2017.08.1591.

Campos-Taberner, M., Moreno-Martinez, A., Garcia-Haro, F.J., Camps-Valls, G., Robinson, N.P., Kattge, J., Running, S.W., 2018. Global estimation of biophysical variables from google earth engine platform. Remote Sens. (Basel) 10 (8). https://doi.org/10.3390/rs10081167.

Camps-Valls, G., Martino, L., Svendsen, D.H., Campos-Taberner, M., Munoz-Mari, J., Laparra, V., Luengo, D., Garcia-Haro, F.J., 2018. Physics-aware gaussian processes in remote sensing. Appl. Soft Comput. 68, 69–82. https://doi.org/10.1016/j.asoc.2018.03.021.

Capolupo, A., Kooistra, L., Berendonk, C., Boccia, L., Suomalainen, J., 2015. Estimating plant traits of grasslands from UAV-acquired hyperspectral images: a comparison of statistical approaches. ISPRS Int. J. Geo Inf. 4 (4), 2792–2820. https://doi.org/10.3390/ijgi4042792.

Casa, R., Jones, H.G., 2004. Retrieval of crop canopy properties: a comparison between model inversion from hyperspectral data and image classification. Int. J. Remote Sens. 25 (6), 1119–1130. https://doi.org/10.1080/01431160310001595046.

Chen, J.M., Black, T.A., 1991. Measuring leaf-area index of plant canopies with branch architecture. Agric. For. Meteorol. 57 (1–3), 1–12. https://doi.org/10.1016/0168-1923(91)90074-Z.

Chen, J.M., Black, T.A., 1992. Defining leaf-area index for non-flat leaves. Plant Cell Environ. 15 (4), 421–429. https://doi.org/10.1111/j.1365-3040.1992.tb00992.x.

Chen, Y.S., Lin, Z.H., Zhao, X., Wang, G., Gu, Y.F., 2014. Deep learning-based classification of hyperspectral data. IEEE J. Sel. Top. Appl. Earth Obs. Remote Sens. 7 (6), 2094–2107. https://doi.org/10.1109/Jstars.2014.2329330.

Chen, Y.S., Jiang, H.L., Li, C.Y., Jia, X.P., Ghamisi, P., 2016. Deep feature extraction and classification of hyperspectral images based on convolutional neural networks. IEEE Trans. Geosci. Remote Sens. 54 (10), 6232–6251. https://doi.org/10.1109/Tgrs.2016.2584107.

Chen, M., Quinnell, R.G., Larkum, A.W.D., 2002. Chlorophyll d as the major photopigment in acaryochloris marina. J. Porphyrins Phthalocyanines 6 (11–12), 763–773. https://doi.org/10.1142/S1088424602000889.

Chu, Z., Yu, J., 2020. An end-to-end model for rice yield prediction using deep learning fusion. Comput. Electron. Agric. 174 https://doi.org/10.1016/j.compag.2020.105471.

Colomina, I., Molina, P., 2014. Unmanned aerial systems for photogrammetry and remote sensing: a review. ISPRS J. Photogramm. Remote Sens. 92, 79–97. https://doi.org/10.1016/j.isprsjprs.2014.02.013.

Combal, B., Baret, F., Weiss, M., 2002. Improving canopy variables estimation from remote sensing data by exploiting ancillary information. case study on sugar beet canopies. Agronomie 22 (2), 205–215. https://doi.org/10.1051/agro:2002008.

Combal, B., Baret, F., Weiss, M., Trubuil, A., Mace, D., Pragnere, A., Myneni, R., Knyazikhin, Y., Wang, L., 2003. Retrieval of canopy biophysical variables from bidirectional reflectance - using prior information to solve the ill-posed inverse problem. Remote Sens. Environ. 84 (1), 1–15. https://doi.org/10.1016/S0034-4257(02)00035-4.

D'Agostino, R., Pearson, E.S., 1973. Tests for departure from normality. empirical results for the distributions of b2 and $\sqrt{b1}$. Biometrika 60 (3), 613–622. https://doi.org/10.2307/2335012.

Dash, J., Curran, P.J., 2004. The MERIS terrestrial chlorophyll index. Int. J. Remote Sens. 25 (23), 5403–5413. https://doi.org/10.1080/0143116042000274015.

Datt, B., 1999. Remote sensing of water content in eucalyptus leaves. Aust. J. Bot. 47 (6), 909–923. https://doi.org/10.1071/Bt98042.

Daughtry, C.S.T., Walthall, C.L., Kim, M.S., de Colstoun, E.B., McMurtrey, J.E., 2000. Estimating corn leaf chlorophyll concentration from leaf and canopy reflectance. Remote Sens. Environ. 74 (2), 229–239. https://doi.org/10.1016/S0034-4257(00)00113-9.

de Sá, N.C., Baratchi, M., Hauser, L.T., van Bodegom, P., 2021. Exploring the impact of noise on hybrid inversion of PROSAIL RTM on Sentinel-2 data. Remote Sens. (Basel) 13 (4). https://doi.org/10.3390/rs13040648.

Dericquebourg, E., Hafiane, A., Canals, R., 2022. Generative-model-based data labeling for deep network regression: application to seed maturity estimation from UAV multispectral images. Remote Sens. (Basel) 14 (20). https://doi.org/10.3390/rs14205238.

Devlin, J., Chang, M.-W., Lee, K., Toutanova, K., 2019. BERT: pre-training of deep bidirectional transformers for language understanding. ArXiv. https://doi.org/10.48550/ARXIV.1810.04805.

Dewi, C., Chen, R.C., 2019. Random forest and support vector machine on features selection for regression analysis. International Journal of Innovative Computing Information and Control 15 (6), 2027–2037. https://doi.org/10.24507/ijicic.15.06.2027.

Domenzain, Luis Mario, Gómez-Dans, José, Lewis, Philip, 2019. Python bindings for the PROSAIL canopy reflectance model.

Dorigo, W.A., 2012. Improving the robustness of cotton status characterisation by radiative transfer model inversion of multi-angular CHRIS/PROBA data. IEEE J. Sel. Top. Appl. Earth Obs. Remote Sens. 5 (1), 18–29. https://doi.org/10.1109/Jstars.2011.2171181.

Du, Y., Jiang, J.B., Liu, Z.W., Pan, Y.Y., 2022. Combining a crop growth model with CNN for underground natural gas leakage detection using hyperspectral imagery. IEEE J. Sel. Top. Appl. Earth Obs. Remote Sens. 15, 1846–1856. https://doi.org/10.1109/Jstars.2022.3150089.

Du, B.J., Mao, D.H., Wang, Z.M., Qiu, Z.Q., Yan, H.Q., Feng, K.D., Zhang, Z.B., 2021. Mapping wetland plant communities using unmanned aerial vehicle hyperspectral imagery by comparing object/pixel-based classifications combining multiple machine-learning algorithms. IEEE J. Selected Topics in Appl. Earth Observations and Remote Sensing 14, 8249–8258. https://doi.org/10.1109/Jstars.2021.3100923.

Duan, S.B., Li, Z.L., Wu, H., Tang, B.H., Ma, L.L., Zhao, E.Y., Li, C.R., 2014. Inversion of the PROSAIL model to estimate leaf area index of maize, potato, and sunflower fields from unmanned aerial vehicle hyperspectral data. Int. J. Appl. Earth Obs. Geoinf. 26, 12–20. https://doi.org/10.1016/j.jag.2013.05.007.

Fabiyi, S.D., Murray, P., Zabalza, J., Ren, J.C., 2021. Folded LDA: extending the linear discriminant analysis algorithm for feature extraction and data reduction in hyperspectral remote sensing. IEEE J. Sel. Top. Appl. Earth Obs. Remote Sens. 14, 12312–12331. https://doi.org/10.1109/Jstars.2021.3129818.

Falster, D.S., Westoby, M., 2003. Leaf size and angle vary widely across species: what consequences for light interception? New Phytol. 158 (3), 509–525. https://doi.org/10.1046/j.1469-8137.2003.00765.x.

Fan, X.H., Liu, C.Y., Liu, S., Xie, Y.Q., Zheng, L.L., Wang, T.C., Feng, Q.P., 2021. The instrument design of lightweight and large field of view high-resolution hyperspectral camera. Sensors 21 (7). https://doi.org/10.3390/s21072276.

Fan, J.H., Zhou, J., Wang, B.W., de Leon, N., Kaeppler, S.M., Lima, D.C., Zhang, Z., 2022. Estimation of maize yield and flowering time using multi-temporal UAV-based hyperspectral data. Remote Sens. (Basel) 14 (13). https://doi.org/10.3390/rs14133052.

Fang, H., Liang, S., 2014. "Leaf Area Index Models." In *Reference Module in Earth Systems and Environmental Sciences*. Elsevier.

Farrell, M.D., Mersereau, R.M., 2005. On the impact of PCA dimension reduction for hyperspectral detection of difficult targets. IEEE Geosci. Remote Sens. Lett. 2 (2), 192–195. https://doi.org/10.1109/Lgrs.2005.846011.

Fei, S.P., Hassan, M.A., Xiao, Y.G., Rasheed, A., Xia, X.C., Ma, Y.T., Fu, L.P., Chen, Z., He, Z.H., 2022. Application of multi-layer neural network and hyperspectral reflectance in genome-wide association study for grain yield in bread wheat. Field Crop Res 289. https://doi.org/10.1016/j.fcr.2022.108730.

Feng, L., Wu, B.H., Chen, S.S., Zhang, C., He, Y., 2022. Application of visible/near-infrared hyperspectral imaging with convolutional neural networks to phenotype aboveground parts to detect cabbage Plasmodiophora brassicae (clubroot). Infrared Phys. Technol. 121 https://doi.org/10.1016/j.infrared.2022.104040.

Foster, A.J., Kakani, V.G., Mosali, J., 2017. Estimation of bioenergy crop yield and N status by hyperspectral canopy reflectance and partial least square regression. Precis. Agric. 18 (2), 192–209. https://doi.org/10.1007/s11119-016-9455-8.

Furbank, R.T., Silva-Perez, V., Evans, J.R., Condon, A.G., Estavillo, G.M., He, W.N., Newman, S., Poire, R., Hall, A., He, Z., 2021. Wheat physiology predictor: predicting physiological traits in wheat from hyperspectral reflectance measurements using deep learning. Plant Methods 17 (1). https://doi.org/10.1186/s13007-021-00806-6.

Gail, P. Anderson, Berk Alexander, K. Acharya Prabhat, W. Matthew Michael, S. Bernstein Lawrence, H. Chetwynd James, Jr., H. Dothe, M. Adler-Golden Steven, J. Ratkowski Anthony, W. Felde Gerald, A. Gardner James, L. Hoke Michael, C. Richtsmeier Steven, Pukall Brian, B. Mello Jason, and S. Jeong Laila. 2000. "MODTRAN4: radiative transfer modeling for remote sensing." Proc.SPIE.

Gao, J.Y., Zhao, L.G., Li, J., Deng, L.M., Ni, J.G., Han, Z.Z., 2021. Aflatoxin rapid detection based on hyperspectral with 1D-convolution neural network in the pixel level. Food Chem. 360 https://doi.org/10.1016/j.foodchem.2021.129968.

Garriga, M., Romero-Bravo, S., Estrada, F., Escobar, A., Matus, I.A., del Pozo, A., Astudillo, C.A., Lobos, G.A., 2017. Assessing wheat traits by spectral reflectance: do we really need to focus on predicted trait-values or directly identify the elite genotypes group? Front. Plant Sci. 8 https://doi.org/10.3389/fpls.2017.00280.

Gitelson, A.A., Kaufman, Y.J., Merzlyak, M.N., 1996. Use of a green channel in remote sensing of global vegetation from EOS-MODIS. Remote Sens. Environ. 58 (3), 289–298. https://doi.org/10.1016/S0034-4257(96)00072-7.

Gitelson, A.A., Merzlyak, M.N., Chivkunova, O.B., 2001. Optical properties and nondestructive estimation of anthocyanin content in plant leaves. Photochem. Photobiol. 74 (1), 38–45. https://doi.org/10.1562/0031-8655(2001)074<0038:Opaneo>2.0.Co;2.

Gitelson, A.A., Gritz, Y., Merzlyak, M.N., 2003. Relationships between leaf chlorophyll content and spectral reflectance and algorithms for non-destructive chlorophyll assessment in higher plant leaves. J. Plant Physiol. 160 (3), 271–282. https://doi.org/10.1078/0176-1617-00887.

Gitelson, A.A., Keydan, G.P., Merzlyak, M.N., 2006. Three-band model for noninvasive estimation of chlorophyll, carotenoids, and anthocyanin contents in higher plant leaves. Geophys. Res. Lett. 33 (11) https://doi.org/10.1029/2006gl026457.

Godoy, J.L., Vega, J.R., Marchetti, J.L., 2014. Relationships between PCA and PLS-regression. Chemom. Intel. Lab. Syst. 130, 182–191. https://doi.org/10.1016/j.chemolab.2013.11.008.

Gomez, C., Lagacherie, P., Coulouma, G., 2008. Continuum removal versus PLSR method for clay and calcium carbonate content estimation from laboratory and airborne hyperspectral measurements. Geoderma 148 (2), 141–148. https://doi.org/10.1016/j.geoderma.2008.09.016.

Grant, L., Daughtry, C.S.T., Vanderbilt, V.C., 1993. Polarized and specular reflectance variation with leaf surface-features. Physiol. Plant. 88 (1), 1–9. https://doi.org/10.1111/j.1399-3054.1993.tb01753.x.

Guanter, L., Kaufmann, H., Segl, K., Foerster, S., Rogass, C., Chabrillat, S., Kuester, T., Hollstein, A., Rossner, G., Chlebek, C., Straif, C., Fischer, S., Schrader, S., Storch, T., Heiden, U., Mueller, A., Bachmann, M., Mühle, H., Müller, R., Habermeyer, M., Ohndorf, A., Hill, J., Buddenbaum, H., Hostert, P., van der Linden, S., Leitao, P.J., Rabe, A., Doerffer, R., Krasemann, H., Xi, H.Y., Mauser, W., Hank, T., Locherer, M., Rast, M., Staenz, K., Sang, B., 2015. The EnMAP spaceborne imaging spectroscopy mission for earth observation. Remote Sens. (Basel) 7 (7), 8830–8857. https://doi.org/10.3390/rs70708830.

Haboudane, D., Miller, J.R., Tremblay, N., Zarco-Tejada, P.J., Dextraze, L., 2002. Integrated narrow-band vegetation indices for prediction of crop chlorophyll content for application to precision agriculture. Remote Sens. Environ. 81 (2–3), 416–426. https://doi.org/10.1016/S0034-4257(02)00018-4.

Hang, R.L., Liu, Q.S., Hong, D.F., Ghamisi, P., 2019. Cascaded recurrent neural networks for hyperspectral image classification. IEEE Trans. Geosci. Remote Sens. 57 (8), 5384–5394. https://doi.org/10.1109/Tgrs.2019.2899129.

He, Z., Liu, H., Wang, Y.W., Hu, J., 2017. Generative adversarial networks-based semi-supervised learning for hyperspectral image classification. Remote Sens. (Basel) 9 (10). https://doi.org/10.3390/rs9101042.

Hedley, J., Roelfsema, C., Phinn, S.R., 2009. Efficient radiative transfer model inversion for remote sensing applications. Remote Sens. Environ. 113 (11), 2527–2532. https://doi.org/10.1016/j.rse.2009.07.008.

Herrmann, I., Karnieli, A., Bonfil, D.J., Cohen, Y., Alchanatis, V., 2010. SWIR-based spectral indices for assessing nitrogen content in potato fields. Int. J. Remote Sens. 31 (19), 5127–5143. https://doi.org/10.1080/01431160903283892.

Hilker, T., Gitelson, A., Coops, N.C., Hall, F.G., Black, T.A., 2011. Tracking plant physiological properties from multi-angular tower-based remote sensing. Oecologia 165 (4), 865–876. https://doi.org/10.1007/s00442-010-1901-0.

Holmgren, W.F., Hansen, C.W., Mikofski, M.A., 2018. pvlib python: a python package for modeling solar energy systems. Ournal of Open Source Software 3 (29):3. https://doi.org/10.21105/joss.00884.

Honkavaara, E., Rosnell, T., Oliveira, R., Tommaselli, A., 2017. Band registration of tuneable frame format hyperspectral UAV imagers in complex scenes. ISPRS J. Photogramm. Remote Sens. 134, 96–109. https://doi.org/10.1016/j.isprsjprs.2017.10.014.

Hou, Q.Y., Wang, Z.L., Su, J.Y., Tan, F.J., 2019. Measurement of equivalent BRDF on the surface of solar panel with periodic structure. Coatings 9 (3). https://doi.org/10.3390/coatings9030193.

Houlsby, Neil, Giurgiu, Andrei, Jastrzebski, Stanislaw, Morrone, Bruna, de Laroussilhe, Quentin, Gesmundo, Andrea, Attariyan, Mona, Gelly, Sylvain, 2019. "Parameter-Efficient Transfer Learning for NLP." International Conference on Machine Learning, Long Beach, California, USA.

Huang, L.S., Ding, W.J., Liu, W.J., Zhao, J.L., Huang, W.J., Xu, C., Zhang, D.Y., Liang, D., 2019. Identification of wheat powdery mildew using in-situ hyperspectral data and linear regression and support vector machines. J. Plant Pathol. 101 (4), 1035–1045. https://doi.org/10.1007/s42161-019-00334-2.

Huang, J.D., He, H.Y., Lv, R.L., Zhang, G.T., Zhou, Z.X., Wang, X.B., 2022b. Non-destructive detection and classification of textile fibres based on hyperspectral imaging and 1D-CNN. Anal. Chim. Acta 1224. https://doi.org/10.1016/j.aca.2022.340238.

Huang, W.J., Niu, Z., Wang, J.H., Liu, L.Y., Zhao, C.J., Liu, Q., 2006. Identifying crop leaf angle distribution based on two-temporal and bidirectional canopy reflectance. IEEE Trans. Geosci. Remote Sens. 44 (12), 3601–3609. https://doi.org/10.1109/Tgrs.2006.881755.

Huang, H., Zhang, B.W., Jing, L.W., Fu, X.H., Chen, X.J., Shi, J.Y., 2022a. Logic tensor network with massive learned knowledge for aspect-based sentiment analysis. Knowl.-Based Syst. 257 https://doi.org/10.1016/j.knosys.2022.109943.

Huete, A.R., Hua, G., Qi, J., Chehbouni, A., Vanleeuwen, W.J.D., 1992. Normalization of multidirectional red and nir reflectances with the savi. Remote Sens. Environ. 41 (2–3), 143–154. https://doi.org/10.1016/0034-4257(92)90074-T.

Huete, A.R., Liu, H.Q., Batchily, K., vanLeeuwen, W., 1997. A comparison of vegetation indices global set of TM images for EOS-MODIS. Remote Sens. Environ. 59 (3), 440–451. https://doi.org/10.1016/S0034-4257(96)00112-5.

Hunt, E.R., Daughtry, C.S.T., Eitel, J.U.H., Long, D.S., 2011. Remote sensing leaf chlorophyll content using a visible band index. Agron. J. 103 (4), 1090–1099. https://doi.org/10.2134/agronj2010.0395.

Jacquemoud, S., Baret, F., 1990. Prospect - a model of leaf optical-properties spectra. Remote Sens. Environ. 34 (2), 75–91. https://doi.org/10.1016/0034-4257(90)90100-Z.

Jakob, S., Zimmermann, R., Gloaguen, R., 2017. The need for accurate geometric and radiometric corrections of drone-borne hyperspectral data for mineral exploration: MEPHySToA toolbox for pre-processing drone-borne hyperspectral data. Remote Sens. (Basel) 9 (1). https://doi.org/10.3390/rs9010088.

Jay, S., Maupas, F., Bendoula, R., Gorretta, N., 2017. Retrieving LAI, chlorophyll and nitrogen contents in sugar beet crops from multi-angular optical remote sensing: comparison of vegetation indices and PROSAIL inversion for field phenotyping. Field Crop Res 210, 33–46. https://doi.org/10.1016/j.fcr.2017.05.005.

Jayaprakash, C., Damodaran, B.B., Viswanathan, S., Soman, K.P., 2020. Randomized independent component analysis and linear discriminant analysis dimensionality reduction methods for hyperspectral image classification. J. Appl. Remote Sens. 14 (3) https://doi.org/10.1117/1.Jrs.14.036507.

Jiang, J.J., Ma, J.Y., Chen, C., Wang, Z.Y., Cai, Z.H., Wang, L.Z., 2018. SuperPCA: a superpixelwise PCA approach for unsupervised feature extraction of hyperspectral imagery. IEEE Trans. Geosci. Remote Sens. 56 (8), 4581–4593. https://doi.org/10.1109/Tgrs.2018.2828029.

Jones, J.W., Hoogenboom, G., Porter, C.H., Boote, K.J., Batchelor, W.D., Hunt, L.A., Wilkens, P.W., Singh, U., Gijsman, A.J., Ritchie, J.T., 2003. The DSSAT cropping system model. Eur. J. Agron. 18 (3–4), 235–265. https://doi.org/10.1016/S1161-0301(02)00107-7.

Ju, C.H., Tian, Y.C., Yao, X., Cao, W.X., Zhu, Y., Hannaway, D., 2010. Estimating leaf chlorophyll content using red edge parameters. Pedosphere 20 (5), 633–644. https://doi.org/10.1016/S1002-0160(10)60053-7.

Kamilaris, A., Prenafeta-Boldu, F.X., 2018. A review of the use of convolutional neural networks in agriculture. J. Agric. Sci. 156 (3), 312–322. https://doi.org/10.1017/S0021859618000436.

Kamilaris, A., Prenafeta-Boldú, F.X., 2018. Deep learning in agriculture: a survey. Comput. Electron. Agric. 147, 70–90. https://doi.org/10.1016/j.compag.2018.02.016.

Kandylakis, Z., Falagas, A., Karakizi, C., Karantzalos, K., 2020. Water stress estimation in vineyards from aerial SWIR and multispectral UAV data. Remote Sens. (Basel) 12 (15). https://doi.org/10.3390/rs12152499.

Kanning, M., Kuhling, I., Trautz, D., Jarmer, T., 2018. High-resolution UAV-based hyperspectral imagery for LAI and chlorophyll estimations from wheat for yield prediction. Remote Sens. (Basel) 10 (12). https://doi.org/10.3390/rs10122000.

Karimi, Y., Parasher, S.O., Madani, A., Kim, S., 2008. Application of support vector machine technology for the estimation of crop biophysical parameters using aerial hyperspectral observations. Can. Biosyst. Eng. 50, 13–20.

Kaufman, Y.J., Tanre, D., 1992. Atmospherically resistant vegetation index (ARVI) for EOS-MODIS. IEEE Trans. Geosci. Remote Sens. 30 (2), 261–270. https://doi.org/10.1109/36.134076.

Kayad, A., Rodrigues, F.A., Naranjo, S., Sozzi, M., Pirotti, F., Marinello, F., Schulthess, U., Defourny, P., Gerard, B., Weiss, M., 2022. Radiative transfer model inversion using high-resolution hyperspectral airborne imagery - retrieving maize LAI to access biomass and grain yield. Field Crop Res 282. https://doi.org/10.1016/j.fcr.2022.108449.

Kedzierski, M., Wierzbicki, D., Sekrecka, A., Fryskowska, A., Walczykowski, P., Siewert, J., 2019. Influence of lower atmosphere on the radiometric quality of unmanned aerial vehicle imagery. Remote Sens. (Basel) 11 (10). https://doi.org/10.3390/rs11101214.

Khan, Z., Rahimi-Eichi, V., Haefele, S., Garnett, T., Miklavcic, S.J., 2018. Estimation of vegetation indices for high-throughput phenotyping of wheat using aerial imaging. Plant Methods 14. https://doi.org/10.1186/s13007-018-0287-6.

Kiranyaz, S., Avci, O., Abdeljaber, O., Ince, T., Gabbouj, M., Inman, D.J., 2021. 1D convolutional neural networks and applications: a survey. Mech. Syst. Sig. Process. 151 https://doi.org/10.1016/j.ymssp.2020.107398.

Klimov, V.V., Klevanik, A.V., Shuvalov, V.A., 1977. Reduction of pheophytin in the primary light reaction of photosystem II. FEBS Lett. 82 (2), 183–186. https://doi.org/10.1016/0014-5793(77)80580-2.

Kobayashi, M., Wang, Z.Y., Yoza, K., Umetsu, M., Konami, H., Mimuro, M., Nozawa, T., 1996. Molecular structures and optical properties of aggregated forms of chlorophylls analyzed by means of magnetic circular dichroism. Spectrochim. Acta Part a-Mol. Biomol. Spectrosc. 52 (5), 585–598. https://doi.org/10.1016/0584-8539(95)01645-7.

Koetz, B., Baret, F., Poilve, H., Hill, J., 2005. Use of coupled canopy structure dynamic and radiative transfer models to estimate biophysical canopy characteristics. Remote Sens. Environ. 95 (1), 115–124. https://doi.org/10.1016/j.rse.2004.11.017.

Koh, J.C.O., Spangenberg, G., Kant, S., 2021. Automated machine learning for high-throughput image-based plant phenotyping. Remote Sens. (Basel) 13 (5). https://doi.org/10.3390/rs13050858.

Koh, J.C.O., Banerjee, B.P., Spangenberg, G., Kant, S., 2022. Automated hyperspectral vegetation index derivation using a hyperparameter optimisation framework for high-throughput plant phenotyping. New Phytol. 233 (6), 2659–2670. https://doi.org/10.1111/nph.17947.

Kong, W.P., Huang, W.J., Zhou, X.F., Song, X.Y., Casa, R., 2016. Estimation of carotenoid content at the canopy scale using the carotenoid triangle ratio index from in situ and simulated hyperspectral data. J. Appl. Remote Sens. 10 https://doi.org/10.1117/1.Jrs.10.026035.

Koppl, C.J., Malureanu, R., Dam-Hansen, C., Wang, S., Jin, H.X., Barchiesi, S., Sandi, J.M. S., Munoz-Carpena, R., Johnson, M., Duran-Quesada, A.M., Bauer-Gottwein, P., McKnight, U.S., Garcia, M., 2021. Hyperspectral reflectance measurements from UAS under intermittent clouds: correcting irradiance measurements for sensor tilt. Remote Sens. Environ. 267 https://doi.org/10.1016/j.rse.2021.112719.

Lamb, D.W., Steyn-Ross, M., Schaare, P., Hanna, M.M., Silvester, W., Steyn-Ross, A., 2002. Estimating leaf nitrogen concentration in ryegrass (lolium spp.) pasture using the chlorophyll red-edge: theoretical modelling and experimental observations. Int. J. Remote Sens. 23 (18), 3619–3648. https://doi.org/10.1080/01431160110114529.

Lambin, E.F., 2001. Remote sensing and geographic information systems analysis. In: Smelser, N.J., Baltes, P.B. (Eds.), International Encyclopedia of the Social & Behavioral Sciences. Pergamon, Oxford, pp. 13150–13155.

Li, J., Cui, R., Li, B., Li, Y., Mei, S., Du, Q., 2019a. Dual 1D–2D spatial-spectral CNN for hyperspectral image super-resolution. IGARSS 2019–2019 IEEE International Geoscience and Remote Sensing Symposium.

Li, X.P., Jiang, H.Z., Jiang, X.S., Shi, M.H., 2021. Identification of geographical origin of chinese chestnuts using hyperspectral imaging with 1D-CNN algorithm. Agriculture-Basel 11 (12). https://doi.org/10.3390/agriculture11121274.

Li, F., Miao, Y.X., Feng, G.H., Yuan, F., Yue, S.C., Gao, X.W., Liu, Y.Q., Liu, B., Ustine, S. L., Chen, X.P., 2014. Improving estimation of summer maize nitrogen status with red

edge-based spectral vegetation indices. Field Crop Res 157, 111–123. https://doi.org/10.1016/j.fcr.2013.12.018.
Li, Y.J., Sun, Y., Jiang, J.M., Liu, J., 2019b. Spectroscopic determination of leaf chlorophyll content and color for genetic selection on sassafras tzumu. Plant Methods 15. https://doi.org/10.1186/s13007-019-0458-0.
Li, P.H., Wang, Q., 2011. Retrieval of leaf biochemical parameters using PROSPECT inversion: a new approach for alleviating ill-posed problems. IEEE Trans. Geosci. Remote Sens. 49 (7), 2499–2506. https://doi.org/10.1109/Tgrs.2011.2109390.
Liang, L., Di, L.P., Zhang, L.P., Deng, M.X., Qin, Z.H., Zhao, S.H., Lin, H., 2015. Estimation of crop LAI using hyperspectral vegetation indices and a hybrid inversion method. Remote Sens. Environ. 165, 123–134. https://doi.org/10.1016/j.rse.2015.04.032.
Liang, L., Qin, Z.H., Zhao, S.H., Di, L.P., Zhang, C., Deng, M.X., Lin, H., Zhang, L.P., Wang, L.J., Liu, Z.X., 2016. Estimating crop chlorophyll content with hyperspectral vegetation indices and the hybrid inversion method. Int. J. Remote Sens. 37 (13), 2923–2949. https://doi.org/10.1080/01431161.2016.1186850.
Liu, X., Wu, J., Chen, S., 2020. "Efficient Hyperparameters optimization Through Model-based Reinforcement Learning and Meta-Learning." 2020 IEEE 22nd International Conference on High Performance Computing and Communications; IEEE 18th International Conference on Smart City; IEEE 6th International Conference on Data Science and Systems (HPCC/SmartCity/DSS), 14-16 Dec. 2020.
Liu, F., Xiao, Z., 2020. Disease spots identification of potato leaves in hyperspectral based on locally adaptive 1D-CNN. 2020 IEEE International Conference on Artificial Intelligence and Computer Applications (ICAICA).
Lo, S.C.B., Chan, H.P., Lin, J.S., Li, H., Freedman, M.T., Mun, S.K., 1995. Artificial convolution neural network for medical image pattern recognition. Neural Netw. 8 (7–8), 1201–1214. https://doi.org/10.1016/0893-6080(95)00061-5.
Loizzo, R., Guarini, R., Longo, F., Scopa, T., Formaro, R., Facchinetti, C., Varacalli, G., 2018. Prisma: the italian hyperspectral Mission. IGARSS 2018–2018 IEEE International Geoscience and Remote Sensing Symposium.
Longbotham, Nathan, Pacifici, Fabio, Malitz, Seth, Baugh, William, Camps-Valls, Gustau, 2015. "Measuring the Spatial and Spectral Performance of WorldView-3." Fourier Transform Spectroscopy and Hyperspectral Imaging and Sounding of the Environment, Lake Arrowhead, California, 2015/03/01.
Lopez-Calderon, M.J., Estrada-Avalos, J., Rodriguez-Moreno, V.M., Mauricio-Ruvalcaba, J.E., Martinez-Sifuentes, A.R., Delgado-Ramirez, G., Miguel-Valle, E., 2020. Estimation of Total nitrogen content in forage maize (Zea mays L.) using spectral indices: analysis by random forest. Agriculture-Basel 10 (10). https://doi.org/10.3390/agriculture10100451.
Lu, Y., 2016. Identification and roles of photosystem II assembly, stability, and repair factors in arabidopsis. Front. Plant Sci. 7 https://doi.org/10.3389/dpls.2016.00168.
Lunagaria, M.M., Patel, H.R., 2019. Evaluation of PROSAIL inversion for retrieval of chlorophyll, leaf dry matter, leaf angle, and leaf area index of wheat using spectrodirectional measurements. Int. J. Remote Sens. 40 (21), 8125–8145. https://doi.org/10.1080/01431161.2018.1524608.
Ma, B.L., Dwyer, L.M., Costa, C., Cober, E.R., Morrison, M.J., 2001. Early prediction of soybean yield from canopy reflectance measurements. Agron. J. 93 (6), 1227–1234. https://doi.org/10.2134/agronj2001.1227.
Ma, Y., Zhang, Y.S., Mei, X.G., Dai, X.B., Ma, J.Y., 2019. Multifeature-based discriminative label consistent K-SVD for hyperspectral image classification. IEEE J. Sel. Top. Appl. Earth Obs. Remote Sens. 12 (12), 4995–5008. https://doi.org/10.1109/Jstars.2019.2949621.
Maimaitijiang, M., Sagan, V., Sidike, P., Hartling, S., Esposito, F., Fritschi, F.B., 2020. Soybean yield prediction from UAV using multimodal data fusion and deep learning. Remote Sens. Environ. 237 https://doi.org/10.1016/j.rse.2019.111599.
Mansuri, S.M., Chakraborty, S.K., Mahanti, N.K., Pandiselvam, R., 2022. Effect of germ orientation during Vis-NIR hyperspectral imaging for the detection of fungal contamination in maize kernel using PLS-DA, ANN and 1D-CNN modelling. Food Control 139. https://doi.org/10.1016/j.foodcont.2022.109077.
Mantilla-Perez, M.B., Fernandez, M.G.S., 2017. Differential manipulation of leaf angle throughout the canopy: current status and prospects. J. Exp. Bot. 68 (21–22), 5699–5717. https://doi.org/10.1093/jxb/erx378.
Meacham-Hensold, K., Montes, C.M., Wu, J., Guan, K.Y., Fu, P., Ainsworth, E.A., Pederson, T., Moore, C.E., Brown, K.L., Raines, C., Bernacchi, C.J., 2019. High-throughput field phenotyping using hyperspectral reflectance and partial least squares regression (PLSR) reveals genetic modifications to photosynthetic capacity. Remote Sens. Environ. 231 https://doi.org/10.1016/j.rse.2019.04.029.
Meng, X., Xie, D.H., Wang, Y., Jia, Y.F., Yan, G.J., 2014. Study on multi-angular polarized Spectrum characteristics of leaf based on some indoor experimental data. Spectrosc. Spectr. Anal. 34 (3), 619–624. https://doi.org/10.3964/j.issn.1000-0593(2014)03-0619-06.
Menon, V., Du, Q., Fowler, J.E., 2016. Fast SVD with random hadamard projection for hyperspectral dimensionality reduction. IEEE Geosci. Remote Sens. Lett. 13 (9), 1275–1279. https://doi.org/10.1109/Lgrs.2016.2581172.
Michel, A.N., 2003. "Recurrent neural networks: overview and perspectives." Proceedings of the 2003 International Symposium on Circuits and Systems, 2003. ISCAS '03., 25-28 May 2003.
Mishra, S., Mishra, D.R., 2012. Normalized difference chlorophyll index: a novel model for remote estimation of chlorophyll-a concentration in turbid productive waters. Remote Sens. Environ. 117, 394–406. https://doi.org/10.1016/j.rse.2011.10.016.
Moazzam, S.I., Khan, U.S., Tiwana, M.I., Iqbal, J., Qureshi, W.S., Shah, S.I., 2019. A review of application of deep learning for weeds and crops classification in agriculture. 2019 International Conference on Robotics and Automation in Industry (ICRAI).
Moghimi, A., Yang, C., Anderson, J.A., 2020. Aerial hyperspectral imagery and deep neural networks for high-throughput yield phenotyping in wheat. Comput. Electron. Agric. 172 https://doi.org/10.1016/j.compag.2020.105299.
Mosqueira-Rey, E., Hernandez-Pereira, E., Alonso-Rios, D., Bobes-Bascaran, J., Fernandez-Leal, A., 2022. Human-in-the-loop machine learning: a state of the art. Artif. Intell. Rev. https://doi.org/10.1007/s10462-022-10246-w.
Mou, L.C., Ghamisi, P., Zhu, X.X., 2017. Deep recurrent neural networks for hyperspectral image classification. IEEE Trans. Geosci. Remote Sens. 55 (7), 3639–3655. https://doi.org/10.1109/Tgrs.2016.2636241.
Nevavuori, P., Narra, N., Lipping, T., 2019. Crop yield prediction with deep convolutional neural networks. Comput. Electron. Agric. 163 https://doi.org/10.1016/j.compag.2019.104859.
Nguyen, T., Brandstetter, J., Kapoor, A., Gupta, J.K., Grover, A., 2023. "ClimaX: A foundation model for weather and climate." International Conference on Machine Learning, Honolulu, HI, USA.
Nguyen, C., Sagan, V., Maimaitiyiming, M., Maimaitijiang, M., Bhadra, S., Kwasniewski, M.T., 2021. Early detection of plant viral disease using hyperspectral imaging and deep learning. Sensors 21 (3). https://doi.org/10.3390/s21030742.
Nichol, C.J., Huemmrich, K.F., Andrew Black, T., Jarvis, P.G., Walthall, C.L., Grace, J., Hall, F.G., 2000. Remote sensing of photosynthetic-light-use efficiency of boreal forest. Agric. For. Meteorol. 101 (2), 131–142. https://doi.org/10.1016/S0168-1923(99)00167-7.
Pak, M., Kim, S., 2017. A review of deep learning in image recognition. 2017 4th International Conference on Computer Applications and Information Processing Technology (CAIPT).
Pan, S.J., Yang, Q.A., 2010. A survey on transfer learning. IEEE Trans. Knowl. Data Eng. 22 (10), 1345–1359. https://doi.org/10.1109/Tkde.2009.191.
Pan, S.J., Tsang, I.W., Kwok, J.T., Yang, Q.A., 2011. Domain adaptation via transfer component analysis. IEEE Trans. Neural Netw. 22 (2), 199–210. https://doi.org/10.1109/Tnn.2010.2091281.
Paoletti, M.E., Haut, J.M., Plaza, J., Plaza, A., 2020. Scalable recurrent neural network for hyperspectral image classification. J. Supercomput. 76 (11), 8866–8882. https://doi.org/10.1007/s11227-020-03187-0.
Paudel, D., Boogaard, H., de Wit, A., Janssen, S., Osinga, S., Pylianidis, C., Athanasiadis, I.N., 2021. Machine learning for large-scale crop yield forecasting. Agr. Syst. 187 https://doi.org/10.1016/j.agsy.2020.103016.
Peng, J.X., Manevski, K., Korup, K., Larsen, R., Andersen, M.N., 2021. Random forest regression results in accurate assessment of potato nitrogen status based on multispectral data from different platforms and the critical concentration approach. Field Crop Res 268. https://doi.org/10.1016/j.fcr.2021.108158.
Pinaya, L., Hugo, W., Vieira, S., Garcia-Dias, R., Mechelli, A., 2020. Convolutional neural networks. In: Mechelli, A., Vieira, S. (Eds.), Machine Learning. Academic Press, pp. 173–191.
Poblete, T., Ortega-Farias, S., Moreno, M.A., Bardeen, M., 2017. Artificial neural network to predict vine water status spatial variability using multispectral information obtained from an unmanned aerial vehicle (UAV). Sensors 17 (11). https://doi.org/10.3390/s17112488.
Pragnere, A., Baret, F., Weiss, M., Myneni, R., Knyazikhin, Y., Wang, L.B., 1999. Comparison of three radiative transfer model inversion techniques to estimate canopy biophysical variables from remote sensing data. IEEE 1999 International Geoscience and Remote Sensing Symposium.
Press, W.H., Teukolsky, S.A., 1990. Savitzky-golay smoothing filters. Comput. Phys. 4 (6) https://doi.org/10.1063/1.4822961.
Qi, J., Chehbouni, A., Huete, A.R., Kerr, Y.H., Sorooshian, S., 1994. A modified soil adjusted vegetation index. Remote Sens. Environ. 48 (2), 119–126. https://doi.org/10.1016/0034-4257(94)90134-1.
Quattoni, A., Collins, M., Darrell, T., 2008. Transfer learning for image classification with sparse prototype representations. 2008 IEEE Conference on Computer Vision and Pattern Recognition.
Raffel, C., Shazeer, N., Roberts, A., Lee, K., Narang, S., Matena, M., Zhou, Y.Q., Li, W., Liu, P.J., 2020. Exploring the limits of transfer learning with a unified text-to-text transformer. J. Mach. Learn. Res. 21.
Raya-Sereno, M.D., Alonso-Ayuso, M., Pancorbo, J.L., Gabriel, J.L., Camino, C., Zarco-Tejada, P.J., Quemada, M., 2022. Residual effect and N fertilizer rate detection by high-resolution VNIR-SWIR hyperspectral imagery and solar-induced chlorophyll fluorescence in wheat. IEEE Trans. Geosci. Remote Sens. 60 https://doi.org/10.1109/Tgrs.2021.3099624.
Rehman, T.U., Ma, D.D., Wang, L.J., Zhang, L.B., Jin, J., 2020. Predictive spectral analysis using an end-to-end deep model from hyperspectral images for high-throughput plant phenotyping. Comput. Electron. Agric. 177 https://doi.org/10.1016/j.compag.2020.105713.
Richardson, A.D., Duigan, S.P., Berlyn, G.P., 2002. An evaluation of noninvasive methods to estimate foliar chlorophyll content. New Phytol. 153 (1), 185–194. https://doi.org/10.1046/j.0028-646X.2001.00289.x.
Riese, F.M., Keller, S., 2019. Soil texture classification with 1D convolutional neural networks based on hyperspectral data. ISPRS Ann. Photogramm. Remote Sens. Spatial Inf. Sci. IV-2/W5:615–621 https://doi.org/10.5194/isprs-annals-IV-2-W5-615-2019.
Roosjen, P.P.J., Suomalainen, J.M., Bartholomeus, H.M., Clevers, J.G.P.W., 2016. Hyperspectral reflectance anisotropy measurements using a pushbroom spectrometer on an unmanned aerial vehicle-results for barley, winter wheat, and potato. Remote Sens. (Basel) 8 (11). https://doi.org/10.3390/rs8110909.
Roosjen, P.P.J., Suomalainen, J.M., Bartholomeus, H.M., Kooistra, L., Clevers, J.G.P.W., 2017. Mapping reflectance anisotropy of a potato canopy using aerial images acquired with an unmanned aerial vehicle. Remote Sens. (Basel) 9 (5). https://doi.org/10.3390/rs9050417.

Roosjen, P.P.J., Brede, B., Suomalainen, J.M., Bartholomeus, H.M., Kooistra, L., Clevers, J.G.P.W., 2018. Improved estimation of leaf area index and leaf chlorophyll content of a potato crop using multi-angle spectral data - potential of unmanned aerial vehicle imagery. Int. J. Appl. Earth Obs. Geoinf. 66, 14–26. https://doi.org/10.1016/j.jag.2017.10.012.

Rouse, J.W., Haas, R.H., Schell, J.A., D.W. SDeering, 1974. Monitoring vegetation systems in the Great Plains with ERTS. 3rd Earth Resources Technology Satellite Symposium.

Ruß, Georg, Brenning, Alexander, 2010. "Data Mining in Precision Agriculture: Management of Spatial Information." Computational Intelligence for Knowledge-Based Systems Design, Berlin, Heidelberg, 2010//.

Sandmeier, S.R., 2000. Acquisition of bidirectional reflectance factor data with field goniometers. Remote Sens. Environ. 73 (3), 257–269. https://doi.org/10.1016/S0034-4257(00)00102-4.

Sandmeier, S., Muller, C., Hosgood, B., Andreoli, G., 1998. Sensitivity analysis and quality assessment of laboratory BRDF data. Remote Sens. Environ. 64 (2), 176–191. https://doi.org/10.1016/S0034-4257(97)00178-8.

Sekrecka, A., Wierzbicki, D., Kedzierski, M., 2020. Influence of the sun position and platform orientation on the quality of imagery obtained from unmanned aerial vehicles. Remote Sens. (Basel) 12 (6). https://doi.org/10.3390/rs12061040.

Selvaraj, M.G., Valderrama, M., Guzman, D., Valencia, M., Ruiz, H., Acharjee, A., 2020. Machine learning for high-throughput field phenotyping and image processing provides insight into the association of above and below-ground traits in cassava (manihot esculentaCrantz). Plant Methods 16 (1). https://doi.org/10.1186/s13007-020-00625-1.

Shaha, M., Pawar, M., 2018. Transfer learning for image classification. 2018 Second International Conference on Electronics, Communication and Aerospace Technology (ICECA), 29-31 March.

Shen, L.Z., Gao, M.F., Yan, J.W., Li, Z.L., Leng, P., Yang, Q., Duan, S.B., 2020. Hyperspectral estimation of soil organic matter content using different spectral preprocessing techniques and PLSR method. Remote Sens. (Basel) 12 (7). https://doi.org/10.3390/rs12071206.

Shu, M.Y., Shen, M.Y., Zuo, J.Y., Yin, P.F., Wang, M., Xie, Z.W., Tang, J.H., Wang, R.L., Li, B.G., Yang, X.H., Ma, Y.T., 2021. The application of UAV-based hyperspectral imaging to estimate crop traits in maize inbred lines. Artn 9890745 Plant Phenomics 2021. https://doi.org/10.34133/2021/9890745.

Siegmann, B., Jarmer, T., 2015. Comparison of different regression models and validation techniques for the assessment of wheat leaf area index from hyperspectral data. Int. J. Remote Sens. 36 (18), 4519–4534. https://doi.org/10.1080/01431161.2015.1084438.

Simonyan, Karen, Zisserman, Andrew, 2015. "Very Deep Convolutional Networks for Large-Scale Image Recognition." International Conference on Learning Representations (ICLR), San Diego.

Singhal, G., Bansod, B., Mathew, L., Goswami, J., Choudhury, B.U., Raju, P.L.N., 2019. Chlorophyll estimation using multi-spectral unmanned aerial system based on machine learning techniques. Remote Sens. Appl.-Soc. Environ. 15 https://doi.org/10.1016/j.rsase.2019.100235.

Song, X., Xu, D.Y., He, L., Feng, W., Wang, Y.H., Wang, Z.J., Coburn, C.A., Guo, T.C., 2016. Using multi-angle hyperspectral data to monitor canopy leaf nitrogen content of wheat. Precis. Agric. 17 (6), 721–736. https://doi.org/10.1007/s11119-016-9445-x.

Su, W., Zhang, M.Z., Bian, D.H., Liu, Z., Huang, J.X., Wang, W., Wu, J.Y., Guo, H., 2019. Phenotyping of corn plants using unmanned aerial vehicle (UAV) images. Remote Sens. (Basel) 11 (17). https://doi.org/10.3390/rs11172021.

Sun, B., Wang, C.F., Yang, C.H., Xu, B.D., Zhou, G.S., Li, X.Y., Xie, J., Xu, S.J., Liu, B., Xie, T.J., Kuai, J., Zhang, J., 2021. Retrieval of rapeseed leaf area index using the PROSAIL model with canopy coverage derived from UAV images as a correction parameter. Int. J. Appl. Earth Obs. Geoinf. 102 https://doi.org/10.1016/j.jag.2021.102373.

Sun, J., Wang, L.C., Shi, S., Li, Z.H., Yang, J., Gong, W., Wang, S.Q., Tagesson, T., 2022. Leaf pigment retrieval using the PROSAIL model: influence of uncertainty in prior canopy-structure information. Crop Journal 10 (5), 1251–1263. https://doi.org/10.1016/j.cj.2022.04.003.

Svendsen, D.H., Martino, L., Campos-Taberner, M., Garcia-Haro, F.J., Camps-Valls, G., 2018. Joint gaussian processes for biophysical parameter retrieval. IEEE Trans. Geosci. Remote Sens. 56 (3), 1718–1727. https://doi.org/10.1109/Tgrs.2017.2767205.

Talukdar, J., Gupta, S., Rajpura, P.S., Hegde, R.S., 2018. "Transfer Learning for Object Detection using State-of-the-Art Deep Neural Networks." 2018 5th International Conference on Signal Processing and Integrated Networks (SPIN), 22-23 Feb. 2018.

Tao, J., Fang, X., 2020. Toward multi-label sentiment analysis: a transfer learning based approach. J. Big Data 7 (1). https://doi.org/10.1186/s40537-019-0278-0.

Thompson, C.N., Guo, W.X., Sharma, B., Ritchie, G.L., 2019. Using normalized difference red edge index to assess maturity in cotton. Crop Sci. 59 (5), 2167–2177. https://doi.org/10.2135/cropsci2019.04.0227.

Thoppilan, Romal, Daniel De Freitas, Jamie Hall, Noam Shazeer, Apoorv Kulshreshtha, Heng-Tze Cheng, Alicia Jin, Taylor Bos, Leslie Baker, Yu Du, YaGuang Li, Hongrae Lee, Huaixiu Steven Zheng, Amin Ghafouri, Marcelo Menegali, Yanping Huang, Maxim Krikun, Dmitry Lepikhin, James Qin, Dehao Chen, Yuanzhong Xu, Zhifeng Chen, Adam Roberts, Maarten Bosma, Vincent Zhao, Yanqi Zhou, Chung-Ching Chang, Igor Krivokon, Will Rusch, Marc Pickett, Pranesh Srinivasan, Laichee Man, Kathleen Meier-Hellstern, Meredith Ringel Morris, Tulsee Doshi, Renelito Delos Santos, Toju Duke, Johnny Soraker, Ben Zevenbergen, Vinodkumar Prabhakaran, Mark Diaz, Ben Hutchinson, Kristen Olson, Alejandra Molina, Erin Hoffman-John, Josh Lee, Lora Aroyo, Ravi Rajakumar, Alena Butryna, Matthew Lamm, Viktoriya Kuzmina, Joe Fenton, Aaron Cohen, Rachel Bernstein, Ray Kurzweil, Blaise Aguera-Arcas, Claire Cui, Marian Croak, Ed Chi, and Quoc Le. 2022. "LaMDA: Language Models for Dialog Applications." *ArXiv*. doi: https://doi.org/10.48550/ARXIV.2201.08239.

Thorp, K.R., Gore, M.A., Andrade-Sanchez, P., Carmo-Silva, A.E., Welch, S.M., White, J.W., French, A.N., 2015. Proximal hyperspectral sensing and data analysis approaches for field-based plant phenomics. Comput. Electron. Agric. 118, 225–236. https://doi.org/10.1016/j.compag.2015.09.005.

Tripathi, R., Sahoo, R.N., Sehgal, V.K., Tomar, R.K., Chakraborty, D., Nagarajan, S., 2012. Inversion of PROSAIL model for retrieval of plant biophysical parameters. J. Indian Soc. Remote Sens. 40 (1), 19–28. https://doi.org/10.1007/s12524-011-0129-8.

Tucker, C.J., Elgin, J.H., McMurtrey, J.E., Fan, C.J., 1979. Monitoring corn and soybean crop development with hand-held radiometer spectral data. Remote Sens. Environ. 8 (3), 237–248. https://doi.org/10.1016/0034-4257(79)90004-X.

Tuia, D., Verrelst, J., Alonso, L., Perez-Cruz, F., Camps-Valls, G., 2011. Multioutput support vector regression for remote sensing biophysical parameter estimation. IEEE Geosci. Remote Sens. Lett. 8 (4), 804–808. https://doi.org/10.1109/Lgrs.2011.2109934.

Verhoef, W., 1984. Light scattering by leaf layers with application to canopy reflectance modeling: the SAIL model. Remote Sens. Environ. 16 (2), 125–141. https://doi.org/10.1016/0034-4257(84)90057-9.

Vina, A., Gitelson, A.A., Nguy-Robertson, A.L., Peng, Y., 2011. Comparison of different vegetation indices for the remote assessment of green leaf area index of crops. Remote Sens. Environ. 115 (12), 3468–3478. https://doi.org/10.1016/j.rse.2011.08.010.

Vogelmann, J.E., Rock, B.N., Moss, D.M., 1993. Red edge spectral measurements from sugar maple leaves. Int. J. Remote Sens. 14 (8), 1563–1575. https://doi.org/10.1080/01431169308953986.

Vollmann, J., Walter, H., Sato, T., Schweiger, P., 2011. Digital image analysis and chlorophyll metering for phenotyping the effects of nodulation in soybean. Comput. Electron. Agric. 75 (1), 190–195. https://doi.org/10.1016/j.compag.2010.11.003.

Vrbančič, G., Podgorelec, V., 2020. Transfer learning with adaptive fine-tuning. IEEE Access 8, 196197–196211. https://doi.org/10.1109/ACCESS.2020.3034343.

Wan, L., Zhang, J.F., Dong, X.Y., Du, X.Y., Zhu, J.P., Sun, D.W., Liu, Y.F., He, Y., Cen, H.Y., 2021. Unmanned aerial vehicle-based field phenotyping of crop biomass using growth traits retrieved from PROSAIL model. Comput. Electron. Agric. 187 https://doi.org/10.1016/j.compag.2021.106304.

Wang, L., Chen, S.S., Peng, Z.P., Huang, J.C.A., Wang, C.Y., Jiang, H., Zheng, Q., Li, D., 2021. Phenology effects on physically based estimation of Paddy Rice canopy traits from UAV hyperspectral imagery. Remote Sens. (Basel) 13 (9). https://doi.org/10.3390/rs13091792.

Wang, W., Cheng, Y.K., Ren, Y., Zhang, Z.H., Geng, H.W., 2022a. Prediction of chlorophyll content in multi-temporal winter wheat based on multispectral and machine learning. Front. Plant Sci. 13 https://doi.org/10.3389/fpls.2022.896408.

Wang, S., Di Tommaso, S., Deines, J.M., Lobell, D.B., 2020. Mapping twenty years of corn and soybean across the US Midwest using the landsat archive. Sci. Data 7 (1). https://doi.org/10.1038/s41597-020-00646-4.

Wang, L. Z., R. Gao, C. C. Li, J. Wang, Y. Liu, J. Y. Hu, B. Li, H. B. Qiao, H. K. Feng, and J. B. Yue. 2023. "Mapping Soybean Maturity and Biochemical Traits Using UAV-Based Hyperspectral Images." *Remote Sensing* 15 (19). doi: ARTN 4807 10.3390/rs15194807.

Wang, Z.H., Zhao, Z., Yin, C.L., 2022b. Fine crop classification based on UAV hyperspectral images and random Forest. ISPRS Int. J. Geo Inf. 11 (4) https://doi.org/10.3390/ijgi11040252.

Weiss, M., Baret, F., Myneni, R.B., Pragnere, A., Knyazikhin, Y., 2000. Investigation of a model inversion technique to estimate canopy biophysical variables from spectral and directional reflectance data. Agronomie 20 (1), 3–22. https://doi.org/10.1051/agro:2000105.

Wu, X.J., Xiao, L.W., Sun, Y.X., Zhang, J.H., Ma, T.L., He, L., 2022. A survey of human-in-the-loop for machine learning. Future Generation Computer Systems-the International Journal of Escience 135, 364–381. https://doi.org/10.1016/j.future.2022.05.014.

Xiang, H.T., Tian, L., 2011. Method for automatic georeferencing aerial remote sensing (RS) images from an unmanned aerial vehicle (UAV) platform. Biosyst. Eng. 108 (2), 104–113. https://doi.org/10.1016/j.biosystemseng.2010.11.003.

Xie, C.Q., Yang, C., 2020. A review on plant high-throughput phenotyping traits using UAV-based sensors. Comput. Electron. Agric. 178 https://doi.org/10.1016/j.compag.2020.105731.

Yang, S.Q., Hu, L., Wu, H.B., Ren, H.Z., Qiao, H.B., Li, P.J., Fan, W.J., 2021. Integration of crop growth model and random forest for winter wheat yield estimation from UAV hyperspectral imagery. IEEE J. Sel. Top. Appl. Earth Obs. Remote Sens. 14, 6253–6269. https://doi.org/10.1109/Jstars.2021.3089203.

Yang, H.B., Hu, Y.H., Zheng, Z.Z., Qiao, Y.C., Zhang, K.L., Guo, T.F., Chen, J., 2022. Estimation of potato chlorophyll content from UAV multispectral images with stacking ensemble algorithm. Agronomy-Basel 12 (10). https://doi.org/10.3390/agronomy12102318.

Yang, G.J., Zhao, C.J., Liu, Q., Huang, W.J., Wang, J.H., 2011. Inversion of a radiative transfer model for estimating forest LAI from multisource and multiangular optical remote sensing data. IEEE Trans. Geosci. Remote Sens. 49 (3), 988–1000. https://doi.org/10.1109/Tgrs.2010.2071416.

Yin, S.Y., Zhou, K., Cao, L., Shen, X., 2022. Estimating the horizontal and vertical distributions of pigments in canopies of ginkgo plantation based on UAV-borne LiDAR, hyperspectral data by coupling PROSAIL model. Remote Sens. (Basel) 14 (3). https://doi.org/10.3390/rs14030715.

Yu, L.H., Shang, J.L., Cheng, Z.Q., Gao, Z.B., Wang, Z.X., Tian, L., Wang, D.T., Che, T., Jin, R., Liu, J.G., Dong, T.F., Qu, Y.H., 2020. Assessment of cornfield LAI retrieved

from multi-source satellite data using continuous field LAI measurements based on a wireless sensor network. Remote Sens. (Basel) 12 (20). https://doi.org/10.3390/rs12203304.

Zarco-Tejada, P.J., Miller, J.R., Noland, T.L., Mohammed, G.H., Sampson, P.H., 2001. Scaling-up and model inversion methods with narrowband optical indices for chlorophyll content estimation in closed forest canopies with hyperspectral data. IEEE Trans. Geosci. Remote Sens. 39 (7), 1491–1507. https://doi.org/10.1109/36.934080.

Zhang, X.Y., Zhao, J.M., Yang, G.J., Liu, J.G., Cao, J.Q., Li, C.Y., Zhao, X.Q., Gai, J.Y., 2019. "Establishment of Plot-Yield Prediction Models in Soybean Breeding Programs Using UAV-Based Hyperspectral Remote Sensing." Remote Sensing 11 (23). doi: ARTN 2752 10.3390/rs11232752.

Zhang, X., Han, L.X., Dong, Y.Y., Shi, Y., Huang, W.J., Han, L.H., Gonzalez-Moreno, P., Ma, H.Q., Ye, H.C., Sobeih, T., 2019a. A deep learning-based approach for automated yellow rust disease detection from high-resolution hyperspectral UAV images. Remote Sens. (Basel) 11 (13). https://doi.org/10.3390/rs11131554.

Zhang, Y., Hui, J., Qin, Q.M., Sun, Y.H., Zhang, T.Y., Sun, H., Li, M.Z., 2021. Transfer-learning-based approach for leaf chlorophyll content estimation of winter wheat from hyperspectral data. Remote Sens. Environ. 267 https://doi.org/10.1016/j.rse.2021.112724.

Zhang, H.K., Li, Y., Zhang, Y.Z., Shen, Q., 2017. Spectral-spatial classification of hyperspectral imagery using a dual-channel convolutional neural network. Remote Sens. Lett. 8 (5), 438–447. https://doi.org/10.1080/2150704x.2017.1280200.

Zhao, W.Z., Du, S.H., 2016. Spectral-spatial feature extraction for hyperspectral image classification: a dimension reduction and deep learning approach. IEEE Trans. Geosci. Remote Sens. 54 (8), 4544–4554. https://doi.org/10.1109/Tgrs.2016.2543748.

Zhou, X., Sun, J., Mao, H.P., Wu, X.H., Zhang, X.D., Yang, N., 2018. Visualization research of moisture content in leaf lettuce leaves based on WT-PLSR and hyperspectral imaging technology. J. Food Process Eng 41 (2). https://doi.org/10.1111/jfpe.12647.

Zhuang, F.Z., Qi, Z.Y., Duan, K.Y., Xi, D.B., Zhu, Y.C., Zhu, H.S., Xiong, H., He, Q., 2021. A comprehensive survey on transfer learning. Proc. IEEE 109 (1), 43–76. https://doi.org/10.1109/Jproc.2020.3004555.